UNIVERSITY OF CALIFORNIA, SAN DIEGO

Information Processing with Longitudinal Spectral Decomposition of Ultrashort Pulses

A dissertation submitted in partial satisfaction of the

requirements for the degree of Doctor of Philosophy

in

Electrical Engineering (Photonics)

by

Robert Elliot Saperstein

Committee in charge:

Professor Yeshaiahu Fainman, Chair
Professor Joseph Ford
Professor William Hodgkiss
Professor Stojan Radic
Professor Lu Sham
Professor Paul K. L. Yu

2007

The Dissertation of Robert Elliot Saperstein is approved, and it is acceptable in quality and form for publication on microfilm:

_____

_____

_____

_____

_____

_____
Chair

University of California, San Diego

2007

DEDICATION

Thank you to all the members of the UNO group with whom I've worked during my time at UCSD. Your friendship is very meaningful, and I wish you all the best. I'd especially like to acknowledge all the occupants of room B507, EBU1. That small space fosters both ideas and smiles. To Professor Fainman, thank you for all of your efforts to support me. Your guidance made this work possible.

This work is dedicated to my parents who made science fun and to my wife, Julia, who makes life fun.

TABLE OF CONTENTS

LIST OF ABBREVIATIONS

A/D	Analog to Digital
AO	Acousto-Optic
AWG	Arrayed Waveguide Grating
CFBG	Chirped Fiber Bragg Grating
CW	Continuous Wave
DCF	Dispersion Compensating Fiber
dB	decibel (unit)
DC	Direct Current (i.e. zero frequency)
DR	Dynamic Range
EDFA	Erbium Doped Fiber Amplifier
EO	Electro-Optic
fs	Femtosecond (unit)
FT	Fourier Transform
FWHM	Full Width at Half Maximum
IF	Intermediate Frequency
IFT	Inverse Fourier Transform
km	Kilometer (unit)
LO	Local Oscillator
ns	Nanosecond (unit)
OCDMA	Optical Code Division Multiple Access
OCT	Optical Coherence Tomography
OFDR	Optical Frequency Domain Reflectometry
OPO	Optical Parametric Oscillator
PMD	Polarization Mode Dispersion
ps	Picosecond (unit)
RF	Radio-Frequency
RIN	Relative Intensity Noise
SDW	Spectral Decomposition Wave
SMF	Single Mode Fiber
SOP	State of Polarization
SPM	Self Phase Modulation
TBWP	Time-Bandwidth Product
μm	Micron (unit)
UWB	Ultra Wideband

LIST OF FIGURES AND TABLE

ACKNOWLEDGEMENTS

The text of Chapter Two, in part or in full, is a reprint of the material as it appears in:

R.E. Saperstein, N. Alic, D. Panasenko, R. Rokitski, Y. Fainman, “Time-Domain Optical Processing using Chromatic Dispersion for Ultrashort Pulse Shaping,” J. Opt. Soc. America B 22, 2247-2436 (2005).

The dissertation author was the primary researcher and author. The co-authors listed in this publication directed and supervised the research that forms the basis for this chapter.

The text of Chapter Three, in part or in full, is a reprint of the material as it appears in:

R. E. Saperstein and Y. Fainman, “Information processing with longitudinal spectral decomposition of ultrafast pulses,” Appl. Opt. **47**, A21-A31 (2008)

The dissertation author was the primary researcher and author. The co-authors listed in this publication directed and supervised the research that forms the basis for this chapter.

The text of Chapter Four, in part or in full, is a reprint of the material as it appears in:

R. E. Saperstein, N. Alic, S. Zamek, K. Ikeda, B. Slutsky, and Y. Fainman, "Processing advantages of linear chirped fiber Bragg gratings in the time domain realization of optical frequency-domain reflectometry," Opt. Express **15**, 15464-15479 (2007).

The dissertation author was the primary researcher and author. The co-authors listed in this publication directed and supervised the research that forms the basis for this chapter.

VITA

Bachelor of Science in Engineering Princeton University	2001
Master of Science in Electrical Engineering (Photonics) University of California, San Diego	2004
Doctor of Philosophy in Electrical Engineering (Photonics) University of California, San Diego	2007

PUBLICATIONS

R. E. Saperstein and Y. Fainman, "Information processing with longitudinal spectral decomposition of ultrafast pulses," Appl. Opt. **47**, A21-A31 (2008)

R. E. Saperstein, N. Alic, S. Zamek, K. Ikeda, B. Slutsky, and Y. Fainman, "Processing advantages of linear chirped fiber Bragg gratings in the time domain realization of optical frequency-domain reflectometry," Opt. Express **15**, 15464-15479 (2007)

R.E. Saperstein, N. Alic, D. Panasenko, R. Rokitski, Y. Fainman, "Time-Domain Optical Processing using Chromatic Dispersion for Ultrashort Pulse Shaping," J. Opt. Soc. America B 22, 2247-2436 (2005).

R.E. Saperstein, D. Panasenko, Y. Fainman, "Demonstration of a microwave spectrum analyzer based on time-domain optical processing in fiber," Opt. Lett., 29, 501-503 (2004).

ABSTRACT OF THE DISSERTATION

Information processing with longitudinal spectral decomposition of ultrashort pulses

by

Robert Elliot Saperstein

Doctor of Philosophy in Electrical Engineering (Photonics)

University of California, San Diego, 2007

Professor Yeshaiahu Fainman, Chair

Optical signal processing with ultrashort pulses allows for the synthesis and analysis of signals at speeds exceeding the limits of conventional electronics. The origin of this processing capability is the large, well-phased bandwidth required to support short optical pulse durations. In comparison with ultrafast optical signals, wideband radio-, micro-, and millimeter wave signals are relatively narrowband and therefore are readily created or detected through optical techniques. Researchers traditionally utilize Fourier synthesis methods to operate on broadband optical signals. Such an approach relies on

decomposing the optical spectrum and manipulating it with a mask or filter. While the spatial domain is most commonly employed for such processing, this approach suffers from slow update speeds and must scale in volume to increase signal complexity. This dissertation explores an alternative approach relying on the decomposition of the optical spectrum of ultrashort pulses in the time domain using chromatically dispersive fiber technologies. The approach is coined longitudinal spectral decomposition in order to contrast with the traditional transverse spectral decomposition.

The dissertation is organized to first familiarize the reader with the toolbox of technologies and signal processing techniques available for the creation and modification of longitudinal spectral decomposition waves. The primary distortion to such processing, associated with higher order dispersion, is introduced and theoretically treated up front. Subsequently, a sequence of applications driven by longitudinal spectral decomposition is presented. These applications include: optical pulse shaping, microwave spectrum analysis and signal generation, as well as high speed optical reflectometry or ranging. By presenting these applications, the dissertation highlights the processing advantages of longitudinal spectral decomposition while also covering a number of subtle issues associated with the method and its supporting technologies.

The goal of the work is to illustrate to the reader the unique capabilities enabled by processing ultrashort pulses in the time domain. Future improvements to broadband optical source generation, dispersive fiber element fabrication, and optical/electrical signal interfacing promise to increase the efficacy of applications relying on longitudinal spectral decomposition and to extend the viability of the technique as a stand-alone processing platform.

Chapter 1

Longitudinal Spectral Decomposition

1.1 Introduction to Fourier Methods in Ultrafast Signal Processing

Ultrafast laser systems are in the midst of a transition from a research technology to a widely available commercial product [1]. The change is driven in large part by the development of modelocked Titanium:Sapphire solid state systems and Erbium-doped fiber systems. Both laser types presently offer turn-key operation, good stability and semi-definable pulse parameters. Supporting nonlinear optical technologies, such as harmonic generators, parametric oscillators and parametric amplifiers, are also commercially available to ensure that pulsed operation is possible at wavelengths throughout the visible and near-infrared regions. With product refinement, it is generally possible for the designer of such laser systems to specify within reasonable values the initial energy, central frequency, temporal duration, and repetition period of the emitted optical pulses. For signal processing the most important characteristic of the short pulse is its ability to effectively probe most optical systems as an impulse or delta function. From an informatics approach [2] to signal generation and detection, means to alter

ultrashort pulses into complicated waveforms that retain the original bandwidth content while expanding the pulse duration through the addition of temporal features are of interest. Because of their broad extent in both temporal and spectral domains, these optical signals are qualitatively and quantitatively described by their large time-bandwidth product (TBWP).

The current speed of arbitrary waveform generation falls well short of permitting the direct synthesis of long-pulsed or continuous optical waveforms with sub-picosecond time features. Equivalently, means do not exist to directly generate correlated optical spectral components with arbitrary complex weights approaching the bandwidths of ultrashort pulses. A more sound approach to creating long duration, broad spectrum signals involves accessing the well defined coherent spectrum of modelocked lasers and altering it to impose desired signal characteristics. Such an approach is coined a Fourier synthesis method due to its relationship to the Fourier treatment of linear systems. It is exactly fair to think of the physical separation of the optical spectrum (known as dispersion) as a type of Fourier transform (FT). The subsequent alteration of spectral (Fourier) coefficients in amplitude or phase is analogous to the imposition of a system transfer function. Recomposing the optical spectrum through another dispersive process, akin to the first but conjugated, is equivalent to the inverse Fourier transform (IFT) operation. Lastly, a shaped temporal waveform is created that, like in linear systems theory, can be thought of as a convolution between the launched pulse and the impulse response of the system. A conceptual graphic of the Fourier synthesis method is shown in Fig. 1.1. Approaches for signal generation and detection are distinguished by whether

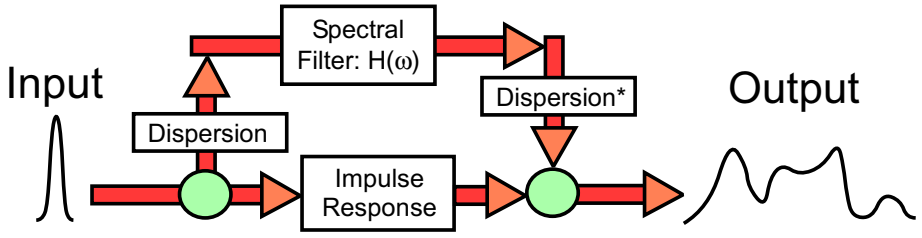

Fig. 1.1: Fourier synthesis method as it applies to the manipulation of short optical pulse waveforms

or not the system transfer function, or equivalently its impulse response, is known *a priori*.

A central question arises then as to how to access and manipulate the optical spectrum in a reconfigurable, dynamic manner. Traditionally, the most popular approach to spectral decomposition relies on space domain processing. Figure 1.2 shows a typically arranged grating-lens pair which maps the incident temporal spectral components to spatial positions at the back focal plane of the lens [3,4]. Throughout this work, this approach is coined transverse spectral decomposition, and the dispersed spectral components are referred to as a spectral decomposition wave (SDW). With the optical spectrum accessible in a single spatial plane, liquid crystal and acousto-optic (AO) modulators provide means for introduction of somewhat arbitrary system transfer functions [5,6]. More recently, compact waveguide-based approaches have used arrayed waveguide gratings (AWGs) to perform an analogous spectral decomposition to those achieved with traditional, free-space coupled gratings [7].

Information processing arrangements using the space domain for transverse spectral decomposition benefit from the maturity of such techniques, the refinement of included components, and the excellent phase control that free-space manipulation provides. Component insensitivity to optical power permits the shaping and detecting of

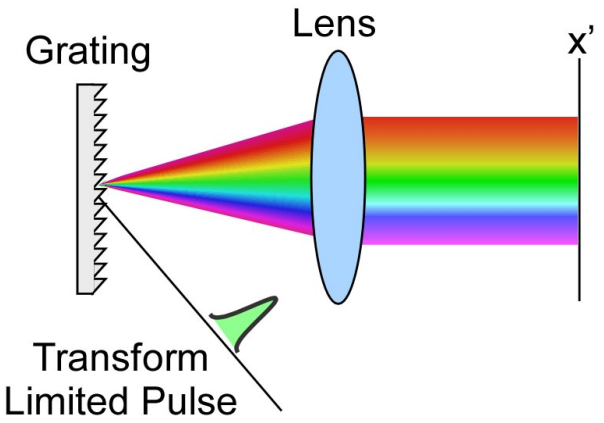

Fig. 1.2: Generation of a transverse SDW in a grating lens pair. The short pulse is spatially dispersed by the grating, while the lens maps the decomposed spectral components to deterministic positions in the spatial plane x'.

high peak power pulses used to drive nonlinear optical systems. Parallelized manipulation of spectral components allows for the concatenation of phase and amplitude masks to readily generate complex coefficients in a transfer function. However, despite the popularity of transverse spectral decomposition, a few key drawbacks motivate the search for alternative means of spectral decomposition and processing. These space domain limitations include the necessity to scale the processor in volume in order to increase the TBWP of generated waveforms, the slow update speeds of reconfigurable spectral masks, and the difficulty of generating single transverse mode outputs due to time/space interrelations [8]. AWG approaches rely on the complex waveguide elements to circumvent large processor volumes and time/space coupling issues, but they too are practically limited by fabrication requirements. The number of resolvable spots in the output waveform for both Fourier synthesis and direct space-to-time AWG approaches [7,9] is equal to the number of waveguide channels. An alternative approach to Fourier processing relying on a single transverse spatial mode can better integrate with fiber

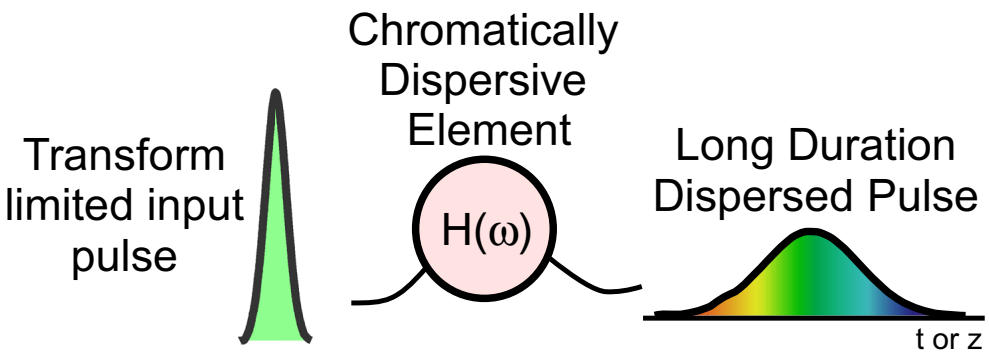

Fig. 1.3: Generation of a longitudinal SDW with a chromatically dispersive element. The spectrum of the propagating pulse decomposes as each component travels with distinct group velocity. The spectrum of the longitudinal SDW is mapped to either position along the optic axis, z, or to time, t.

systems and photonic lightwave circuits and will scale in length only for the achievement of large TBWPs.

Fiber-based and fiber-integrated processors can manipulate optical waveforms in the time domain exploiting chromatic dispersion to generate an alternative form of SDW. As a pulse propagates in dispersive single mode fiber media, each chromatic component travels with its own group velocity and therefore is mapped to a unique temporal position under the expanded pulse envelope. Throughout the manuscript we refer to this temporal dispersion approach as longitudinal spectral decomposition and the generated waveform as a longitudinal SDW, see Fig. 1.3. Drawing on the identical mathematical treatments of diffraction in space and dispersion in time [10], an approximate FT of an incident optical signal is achieved via chromatic dispersion after reaching the so called, "far-field approximation." With such an amount of dispersion, the temporal waveform closely resembles the spectrum [11]. Similar to transverse SDWs, longitudinal SDWs are compatible with Fourier synthesis approaches. As opposed to the space-variant elements discussed above, a single mode time-variant element (e.g. modulator) filters the

temporally dispersed spectrum. The distinction is significant as the transfer function in longitudinal systems may be easily updated on a pulse-to-pulse basis. It is additionally possible to recompose the dispersed optical spectrum through propagation in a conjugate dispersion source matched (i.e. of opposite sign but equal magnitude) to the first dispersive element. The creation of large TBWP waveforms using longitudinal processing relies on both a suitable temporal modulation scheme and the experimental ability to disperse a sub-picosecond pulse using second-order dispersion. The demands of this temporal approach are markedly simpler to implement than the scaling requirements for transverse SDW processors, where larger volume and larger array modulation filters are necessary for TBWP increases.

1.2 Dissertation Thesis and Outline

Due to its potential for large TBWP signal generation and detection, longitudinal spectral decomposition of ultrashort pulses is an important technique for high speed optical processing. To date demonstrations of the longitudinal approach have been shown in: optical pulse shaping [12-14],[17–19] microwave spectrum analysis [15],[20] microwave signal generation [16-18],[21,24,23] temporal signal magnification [19,20],[22,25], coherent Raman spectroscopy [21,22],[26,27] intra-cavity modelocked laser chirped pulse amplification [23], optical coherence tomography/ reflectometry [24-26], and for optical communications: coherent code division multiple access encoding/decoding [27],[28] and delay buffering [28,29].[29,30] Each of these example works relies on longitudinal spectral decomposition as the underlying operating principle for signal processing. Their results would not be achievable using conventional space domain techniques for transverse

SDW generation. Furthermore, it is important to note that longitudinal SDW is an evolving technique. Each of the applications mentioned would show greater processing power were the constituent, underlying technologies enabling longitudinal spectral decomposition to improve in merit. Thus the future of longitudinal SDW processing is optimistic. Significant processing improvements and new applications for the technique will accompany further study.

This dissertation is organized to first familiarize the reader with the theoretical treatment and practical implementation of longitudinal SDWs. Three specific applications are then discussed in details that highlight the advantages and challenges of processing with longitudinal SDWs.

Chapter 1 introduces the dissertation before uncovering the specifics of longitudinal spectral decomposition. The treatment of the dispersion technique is two-fold: first the mathematics describing dispersive propagation of ultrafast pulses is covered in both time and frequency domains. The operating principle and main source of aberration are discussed. Subsequently, the toolbox of accessible technologies available to a researcher wishing to generate and manipulate longitudinal SDWs is introduced and categorized.

Chapter 2 covers the application of longitudinal SDW processing to the realization of an ultrafast pulse shaping system. Optical waveform synthesis is demonstrated. Additionally, the impact of practical limitations imposed by higher order chromatic dispersion are theoretically treated and matched to experimental results.

Chapter 3 demonstrates the utility of ultrafast optical signal processing using longitudinal spectral decomposition in the area of microwave photonics. Specifically,

processing techniques are developed for both the detection and synthesis of microwave signals. Again the role of higher order dispersion as a performance limitation is discussed.

Chapter 4 covers the utilization of chromatic dispersion to map the technique of optical frequency domain reflectometry to the time domain. Implications for high speed data acquisition are detailed. Distortion correction permits high resolution depth imaging at all ranges, while an advanced dispersion technology is shown to enhance signal processing capabilities through the isolation of target position and velocity information.

Chapter 5 presents a summary for the dissertation and outlines future directions and applications for longitudinal spectral decomposition.

1.3 Theoretical Treatment of Longitudinal Spectral Decomposition

Longitudinal spectral decomposition provides a means to access and operate on the spectral components of broadband optical pulses in a single mode, time-of-flight operation. Ignoring system loss, physical pulse propagation in a chromatically dispersive medium is described through the accumulation of spectral phase. A sub-picosecond transform limited pulse at *z=0* with its complex spectral amplitude, $U(0,\omega)$, propagates along the *z*-axis of an optical fiber with propagation constant $\beta(\omega)$, described by a Taylor expansion [4],

$$\beta(\omega) = \beta_0 + \beta_1\omega + 1/2\,\beta_2\omega^2 + 1/6\,\beta_3\omega^3 + \ldots, \tag{1.1}$$

yielding complex spectral amplitude at distance z,

$$U(z,\omega) = U(0,\omega)\exp\left(-j\beta_1\omega\right)\exp\left(-j\frac{1}{2}\beta_2 z\omega^2\right)\exp\left(-j\phi\left(\omega\right)\right). \qquad (1.2)$$

Here ω represents a shifted spectrum around the carrier frequency, i.e. $\omega=\Omega-\omega_c$ if Ω is absolute frequency. The constant phase term with coefficient β_0 is typically ignored, and the linear phase term with the coefficient β_1 causes a simple group delay of the pulse relating to the group velocity of the carrier frequency. The quadratic spectral phase represents the phase term of interest for generating longitudinal SDWs. The strength of the quadratic phase is seen to depend on the value of the coefficient β_2, and on the propagation length z. In the fiber media of interest to longitudinal spectral decomposition, this quadratic term dominates all higher order terms, which are collected into a single phase term, $\phi\left(\omega\right)$. As the system is linear, time-invariant, Eq. (1.2) should be considered as a transfer function, $H(\omega)$, description for pulse propagation,

$$\begin{aligned} U(z,\omega) &= U(0,\omega)H(\omega)\exp\left(-j\phi(\omega)\right) \\ &= U_1(0,\omega)H(\omega) \end{aligned}. \qquad (1.3)$$

A new spectral amplitude, $U_1(0,\omega)$, is introduced in Eq. (1.3) that contains the launch pulse spectrum and the higher order phase terms grouped together. As a result, the pulse, $U_1(0,\omega)$, contains the spectral phase of the pulse at fiber launch added to the spectral phase induced by higher order dispersion.

In the time-domain, dispersive pulse propagation is characterized through an impulse response. The transfer function, $H(\omega)$, has a well known temporal response given by:

$$h(t') = h_0 \exp\left(j \frac{t'^2}{2\beta_2 z} \right). \tag{1.4}$$

Here t' represents time in the moving reference frame of the pulse such that $t' = t - \beta_1 z$. The scaling term equals, $h_0 = 1/\sqrt{j2\pi\beta_2 z}$. Thus the time domain expression corresponding to Eq. (1.3) is $u(z,t') = h(t') \otimes u_1(0,t')$, which can be written out with the full convolution integral as:

$$\begin{aligned} u(z,t') &= h_0 \int_{-\Delta/2}^{\Delta/2} u_1(0,t'') \exp\left(j \frac{(t'-t'')^2}{2\beta_2 z} \right) dt'' \\ &= h_0 \exp\left(j \frac{t'^2}{2\beta_2 z} \right) \int_{-\Delta/2}^{\Delta/2} u_1(0,t'') \exp\left(j \frac{t''^2}{2\beta_2 z} \right) \exp\left(-j \frac{t't''}{\beta_2 z} \right) dt'' \end{aligned}. \tag{1.5}$$

where Δ is the duration of the pulse $u_1(0,t')$. Note that Δ approaches the transform limited duration of $u(0,t')$ if the higher order phase terms are significantly small. Furthermore the Fresnel integral of Eq. (1.5) relaxes with the so called "far field approximation" when the condition $|\beta_2 z| \gg \Delta^2/2$ is satisfied. This Fraunhofer-like approximation highlights the mathematical analog between dispersive pulse propagation and diffractive free space propagation [10]. In the far-field regime the time domain signal envelope represents the spectral amplitude closely and has an instantaneous carrier frequency varying linearly with time under the envelope,

$$\begin{aligned} u(z,t') &= h_0 \exp\left(j \frac{t'^2}{2\beta_2 z} \right) \int_{-\Delta/2}^{\Delta/2} u_1(0,t'') \exp\left(-j \frac{t't''}{\beta_2 z} \right) dt'' \\ &= h_0 \exp\left(j \frac{t'^2}{2\beta_2 z} \right) U_1(0,\omega')\Big|_{\omega' = t'/\beta_2 z} \end{aligned}. \tag{1.6}$$

Note that the approximate Fourier transform maps the spectral content to time using the relationship $\omega' = {t'}/{\beta_2 z}$. The far-field condition, $|\beta_2 z| \gg \Delta^2/2$, thus indicates the propagation requirements needed to achieve a longitudinal SDW in the time-domain. As an example with dispersion in SMF of $\beta_2 = -20\ \mathrm{ps}^2/\mathrm{km}$ and pulses of about 0.1 ps duration, the far field is achieved within only a few meters of fiber (when higher order effects are as of yet negligible).

Higher order dispersion is occasionally physically absent from a processor or assumed absent to facilitate conceptual understanding in system descriptions. In these cases, the pulse $U_1(0,\omega)$ can be replaced by $U(0,\omega)$ in the time and spectral domain signals of Eq. (1.6) and Eq. (1.3), respectively. However, in general, higher order dispersion is the principle aberration to all longitudinal SDW processors. Specifically, for low loss operation in the conventional telecommunications operation band around 1550nm with initial pulse durations longer than 100 fs, β_3 proves to be the dominant distortion term. To gain insight into the impact of higher order dispersion on applications discussed in this dissertation, Eq. (1.2) will be commonly modified to reflect only the cubic spectral phase as,

$$U(z,\omega) = U(0,\omega)\exp(-j\beta_0)\exp(-j\beta_1 z\omega)\exp\left(-j\frac{1}{2}\beta_2 z\omega^2\right)\exp\left(-j\frac{1}{6}\beta_3 z\omega^3\right). \qquad (1.7)$$

Further higher order terms can be returned easily but are neglected to promote simplicity in the analytical treatment. In the time domain description of the longitudinal SDW in Eq. (1.6), the approximate FT implies that the higher order spectral phase terms are mapped into temporal phase terms using $\omega' = {t}/{\beta_2 z}$. Thus the cubic spectral phase of β_3 is also

a temporal cubic phase contributing to the instantaneous carrier frequency. Recalling the definition of spectral group delay, $D(\omega) = -\partial\left[\beta(\omega)z\right]/\partial\omega$, the general result of higher order dispersion terms is the contribution of spectral delays with quadratic, cubic, and higher descriptions. The generated longitudinal SDWs no longer enjoy the simple linear mapping of frequency components to temporal position. The specific impact of the distortion is application dependent and will be treated through the technological applications introduced in subsequent chapters.

1.4 Practical Realization of Longitudinal Spectral Decomposition

Single mode fiber technologies allow for the practical implementation of longitudinal SDW processors. Table 1.1 details a list of useful components and their processing role. Chromatic dispersion is commonly accumulated for the creation of longitudinal SDWs from ultrashort pulses through propagation in single mode fibers or in chirped fiber Bragg gratings (CFBG). SMF and dispersion compensating fiber (DCF) are the most easily obtained dispersion sources, and when they are matched to one another, they allow an operator to create conjugated spectral phase signals (i.e. signals with a flipped sign in the spectral phase). In conjunction, SMF and DCF can be used to create a longitudinal SDW and then recompress the signal back to transform limit. However, these dispersive media contain higher order dispersion, and a theoretical treatment of a system to which they contribute must follow from Eq. (1.7). An important figure of merit for any dispersion medium is its dispersion-loss ratio. This figure is deduced for fibers by dividing the dispersion per unit length by the loss per unit length. As is listed in Table

1.1, SMF and DCF perform well, with DCF showing a clear advantage. This result, in addition to the favorable nonlinear optical properties of DCF, motivates the use of DCF in fiber applications requiring large accumulated dispersion.

CFBG dispersion technology offers additional flexibility and performance benefits to longitudinal SDW processing approaches. CFBG devices are based on longitudinally space-variant gratings written into the core of optical fiber [30]. To create substantial group velocity dispersion, the period of the grating is varied over the duration of the grating. As the Bragg condition for reflection is period dependent, individual wavelengths reflect at unique points along the grating length and accumulate distinct group delays. The space variance of the grating challenges the definition of a global propagation constant as was done for general dispersive media propagation in Eq. 1.1. For analytical treatment of longitudinal SDWs reflected from CFBGs, it is more sensible to describe the resultant spectral phase, $\Phi(\omega)$, through a Taylor expansion. Treating the phase $\Phi(\omega)$ as we did the $\beta(\omega)z$ product above, the resultant dispersed pulse has spectral amplitude,

$$U(z,\omega) = U(0,\omega)\exp(-j\Phi_0)\exp(-j\Phi_1\omega)\exp\left(-j\frac{1}{2}\Phi_2\omega^2\right)\exp\left(-j\phi(\omega)\right). \quad (1.8)$$

In practice CFBGs are lithographically defined with writing techniques that continue to improve. Today commercially available gratings offer differential group delays well in excess of 100 ps (shortest path to longest path delay relates to grating length) [31-33]. Gratings also offer the benefits of low loss, low latency, short interaction length, and small footprint. Note the dispersion to loss figure of merit deduced from two commercial manufacturers. The factor of 10 improvement from the Proximion product with respect

Table 1.1: Processing Elements for Longitudinal SDWs

Technology	Contribution	Advantage	Drawback	Dispersion to loss Ratio
SMF *SDW generator*	Spectral phase filter	Broadband; easily trimmed in length	Higher order dispersion terms present	100 ps^2/dB
DCF *SDW generator*	Conjugate spectral phase filter, matched to SMF (opposite sign)	Like SMF + no soliton support & lower loss per unit dispersion	Higher order dispersion terms present	300 ps^2/dB
CFBG *SDW generator*	Quadratic spectral phase filter, choice of sign for phase	Can be written without higher order dispersion; very low loss per unit dispersion	Amplitude and phase ripple are present; birefringence limits compatibility with modulators	1000ps^2/dB (Proximion) 100ps^2/dB (3M Corp)
Modulators	High speed mixer; Contributes temporal phases	Spectral phase and intensity manipulation; provides frequency shifts to SDW;	Time-variant elements require synchronization with incoming signal	N/A
Temporal Delay Lines	Linear spectral phase filter	Due to the mapping of frequency to time, this filter works similarly to a freq. shifter	Generally performed in free space for ease of tuning	N/A

to the 3M Corp. product results from the fact that the Proximion grating is 10 times greater in length (i.e. more dispersive). The majority of loss involved in CFBG dispersion comes from the one time loss in the supporting fiber components: circulator, couplers, etc. By extending the CFBG's length, Proximion dramatically improved performance in this figure of merit to a point that is easily unmatched by other fiber technologies. A number of works have demonstrated passive optical pulse shaping through the use of superstructures and spectral filters written directly into fiber Bragg

gratings [34-37]. The most important impact for longitudinal SDW processing is that CFBGs can be written to eliminate higher order dispersion terms. When using spectrally tailored CFBGs, the resulting complications of β_3 can subside and the phase term, $\phi(\omega)$, of Eq. (1.8) can be ignored. Experimental evidence of the improved linearity of dispersion performance of CFBGs with respect to SMF is shown experimentally in Chapter 3. As an additional benefit to processor design, when access is available to both sides of the grating, one can easily create time-reversed, conjugated SDWs by reflecting from both the red and blue ends.

The deployment of CFBG technology for SDW generation is slowed by several technical challenges stemming from current fabrication methods. It is important to note that SMF and DCF development and fabrication techniques are greatly aided by their widespread usage by the telecommunications industry. CFBGs have a much smaller market placement and are accordingly slower to develop. Physically, in CFBGs the achievable grating length limits total optical bandwidth and dispersion strength. This length figure is currently capped at roughly 10 meters in state-of-the-art fabrication [32]. Phase and amplitude ripple induced by the writing process may place a limit on achievable dynamic range in some longitudinal SDW processing methods. Phase ripple specifically acts as a measurable contributor to the higher order phase term, $\phi(\omega)$. However, the deterministic phase and amplitude ripple in practice can be made substantially smaller than the higher order dispersion contributions arising in the competing technologies of SMF and DCF.

The most restrictive issue impeding the widespread utilization of CFBGs in longitudinal SDW techniques is the well known problem of their birefringence [16,38].

This birefringence is fundamental and is induced during the writing process. Because each region of the grating is responsible for reflecting a different spectral component, the output longitudinal SDW suffers from spectrally dependent polarization rotation or multi-order polarization mode dispersion (PMD). To give a sense for the magnitude of the problem, Fig. 1.4 presents a study conducted to determine the strength of spectral polarization rotation from SMF, DCF, and CFBGs. The simplistic setup is shown in Fig. 1.4(a). Here a tunable wavelength continuous wave (CW) source with stationary polarization is launched into the dispersive device. The state of polarization (SOP) for the output wave is measured using a commercial test and measurement device and then plotted as the wavelength is tuned. The SOP is depicted using the measured Stokes parameters [39]. The Stokes parameters correspond to the following physical properties of the wave: S0 gives the total incident power (not shown), S1 gives the amount of linear polarization in the horizontal (+1) or vertical (-1) directions, S2 gives the amount of linear polarization in the +45˚ (+1) or -45˚ (-1) directions, while S3 gives the amount of right hand circular (+1) or left hand circular (-1) polarization. As presented, s1, s2, and s3 are the values of S1, S2, and S3 normalized by S0. The degree of polarization is not shown because coherence is preserved in the measurement. The most important result depicted in Fig. 1.4 is the variance of the Stokes parameters versus wavelength for the four dispersion devices. This variation quantifies the polarization rotation across the spectral/temporal extent of a generated longitudinal SDW. Fig. 1.4(b) shows the results for a 10km span of SMF providing 200ps^2 of dispersion. A 3km span of DCF giving 360 ps^2 of dispersion is shown in Fig. 1.4(c). Note that the variance at the DCF output is much smaller despite the larger dispersion value. Higher order polarization rotation (and

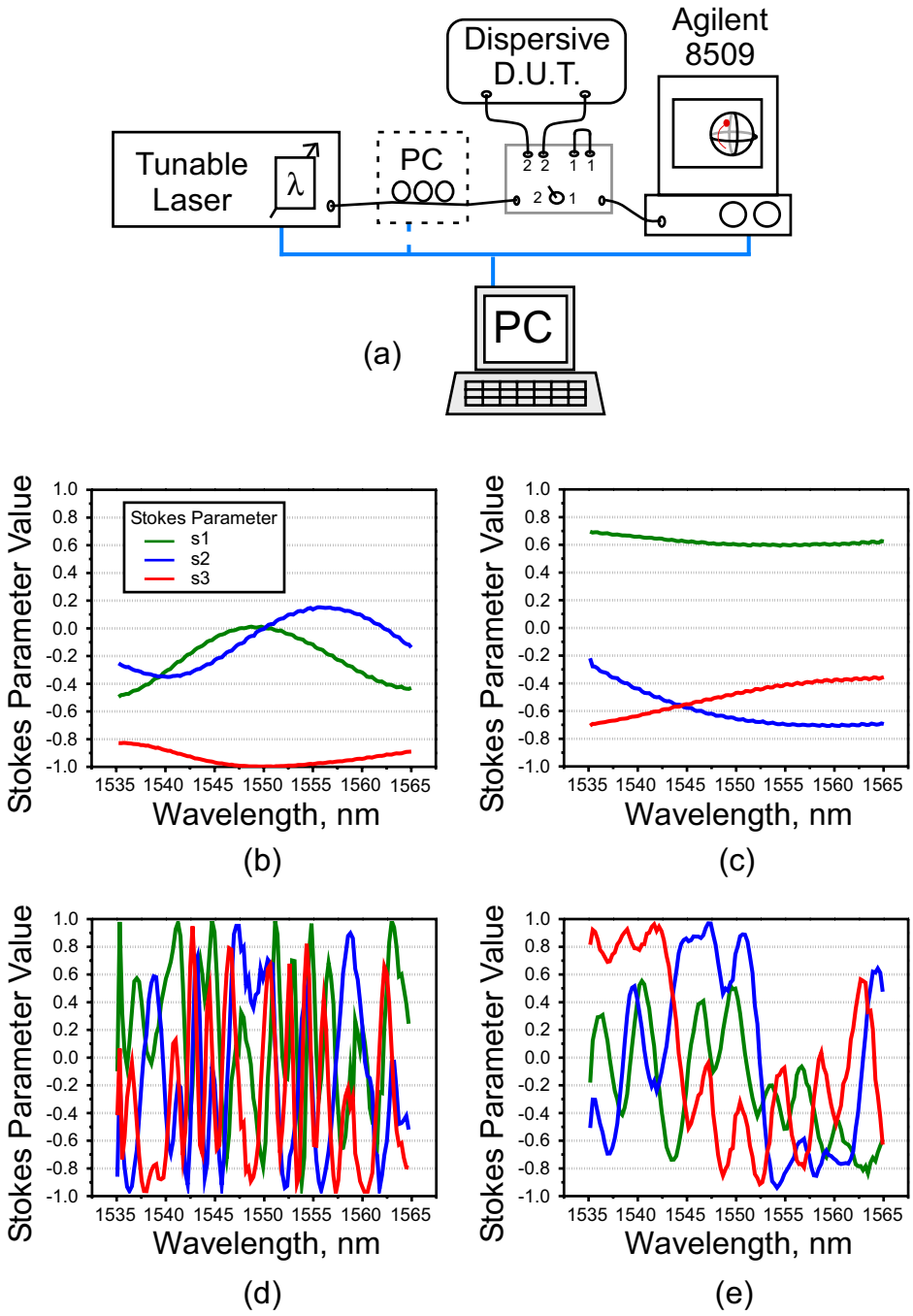

Fig. 1.4: Study of polarization rotation across the bandwidth of interest for signals propagating through chromatically dispersive media of interest. For each medium, a frequency tunable CW source is swept from 1535 to 1565 nm and the output SOP is captured via the Stokes Parameters, see (a). s1, s2, and s3 are plotted versus wavelength. (b) 10.5 km of SMF fiber (c) 3km of DCF corresponding to ~18 km of SMF. DCF clearly has a performance edge to SMF. (d) 3M CFBG shows dramatic polarization rotation while (e) the Proximion grating shows a slightly reduced effect due to an alternative fabrication process.

PMD in general) scales with propagation length in commercial fibers. Fig. 1.4(d) shows the dramatic results for a 3M Corp. 1.1 meter CFBG. Fig. 1.4(e) lastly shows the result for the 10 meter Proximion CFBG. The slightly improved performance by the newer Proximion grating with respect to the 3M grating is principally attributed to the improved lithographic writing process used.

Compensating for the polarization rotation within a generated longitudinal SDW proves experimentally very challenging. It requires either a very fast time domain polarization rotator or fine stress modifications to the grating. The net result of higher order PMD is the poor efficacy of any subsequent polarization dependent device or process. The most important limitation in the systems included in this dissertation is the incompatibility of longitudinal SDWs from CFBGs with electro-optic (EO) modulators, whose role is introduced below. For use of CFBG induced SDWs with these devices, polarization variation results in both spectrally-dependent transmittance and spectrally-dependent modulation depth. In order to freely use linear CFBGs to improve the performance of longitudinal SDW processors, a method for complete PMD mitigation through improved CFBG design is needed. A potential solution under current investigation is the use of highly birefringent polarization maintaining fibers within CFBGs. At present, the optical reflectometry technique discussed in Chapter 4 is the only application introduced in this dissertation capable of taking advantage of CFBG technology due to its lack of required active EO modulation.

A time-variant element is required to operate on the dispersed temporal spectral components of the longitudinal SDW. Fortunately, due to its basis in fiber technologies, longitudinal SDW processing is fundamentally compatible with advanced fiber-coupled

EO and acousto-optic (AO) modulators. With their broad industrial utilization, these modulators are reasonably priced and widely available. EO modulation technology currently pushes toward 100 GHz operation implying that a large number of manipulations can be made to the optical spectrum of a longitudinal SDW of nanosecond to microsecond scale duration. Note that operation bandwidths for modulator devices are limited to roughly 40nm around 1550nm implying a compatibility issue with modelocked pulses originating at sub-100fs duration. While intensity modulation of the optical spectrum is possible with temporal modulators, the frequency shifts associated with intensity and phase-only modulation are experimentally most relevant to the processor. Theoretically, modulation frequencies contribute temporal linear phases to the time domain SDW. To complement these temporal phase terms, additional phase manipulation is possible via signal delay, see Table 1.1. Controllable delays produce a tunable linear phase in the spectral domain for the SDW. However, the mapping of frequencies to time through the FT relationship shown in Eq. (1.6) implies an ambiguity or coupling between the temporal and spectral linear phases. Except near the margins of the signal bandwidth, delays and frequency shifts to longitudinal SDWs prove indistinguishable. Fig. 1.5 offers a visualization of the coupling between these two types of phase shifts. The graph utilizes a time-frequency plotting that is formally akin to a Wigner distribution [40, 41]. For reference, the transform limited pulse emitted from a modelocked laser is shown in Fig. 1.5 (a). Fig. 1.5 (b) shows a dispersed pulse, which can be seen to occupy the same bandwidth as the transform limited pulse, while extending over a much greater time duration, i.e. the TBWP increased significantly. Fig. 1.5 (c) shows the coupling effect between linear phases in time and spectrum. Note that

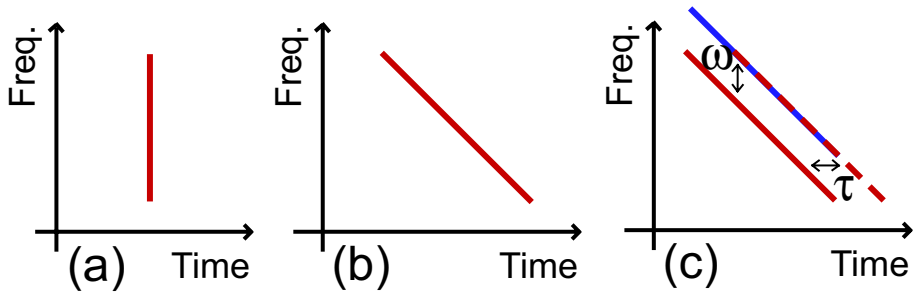

Fig. 1.5: Time-frequency visualizations of (a) transform limited pulse (b) dispersed pulse making a longitudinal SDW and (c) the ambiguity between time and frequency shifts for longitudinal SDWs.

the presence of significant higher order dispersion will bend the line representing the pulse on this plot, leading to a break in the degeneracy of temporal and spectral shifts. While it may initially appear as a problem, the ambiguity of linear temporal and spectral phases will play a key role in all signal processing demonstrations presented in this dissertation.

Chapter 2

Optical Pulse Shaping with Longitudinal Spectral Decomposition

2.1 Introduction

A number of science and engineering applications, including coherent quantum control and optical communications, motivate research in optical pulse shaping [42,43]. Fourier synthesis methods are broadly implemented to achieve desired shaped pulsed waveforms with sub-picosecond temporal features. In such an approach the produced optical signal is composed of a waveform proportional to the input pulse convolved with the FT of an applied spectral filter. As detailed in Chapter 1, the space domain is traditionally used to perform waveform synthesis. A pair of gratings and lenses or a compact AWG arrangement is used to decompose and compose the spectral content of the pulsed, optical waveforms. Pulse shaping arrangements using the space domain for transverse spectral decomposition offer excellent phase manipulation for applications performing quantum control. Furthermore, nonlinear optical elements can be introduced directly into these processors to provide unique ultrafast waveform synthesis capabilities

with response times in the range of femtoseconds [44-51]. These spatial processing approaches have limitations, however, when creating waveforms for optical communications. Coupling shaped waveforms back into a single mode fiber introduces loss and limits the temporal extent of generated pulse shapes. The origin of this restraint is the time/space interrelation inherent in traditional pulse shaping devices [8]. Spatial-temporal pulse shapers utilizing diffraction gratings and lenses have a spatial offset between advanced and delayed pulses in the transverse mode of the output optical waveform. Subsequent launch into the output fiber windows the spatial mode and thus also windows the created pulse shape in time. AWG approaches rely on complicated waveguide elements to circumvent this problem but are fabrication limited in the total number of waveguide channels. This chapter shows that an alternative approach to pulse shaping relying on longitudinal spectral decomposition can operate in a single transverse mode, fully integrated with fiber systems.

The fiber-based, sub-picosecond pulse shaping technique is a natural fit for optical communications applications owing to its origins in and reliance upon optical telecommunications equipment and devices. After creating a dispersion induced longitudinal SDW, fiber coupled modulators are available to perform spectral filtration while conjugate dispersive fiber sources, matched to the first, can recomposes the pulsed waveform. This practical layout can be thought of in communications terms as a dispersion compensated link (with additional modulator). In the Fourier synthesis approach, the potential number of resolvable spots, i.e. TBWP, of the generated waveform relies on the modulation speed and the experimental ability to stretch and recompress a sub-picosecond pulse using second-order dispersion. A system designer

has the ability to vary the propagation distance or the strength of the second order dispersion parameter in order to linearly affect the time duration of the SDW. Decreasing the temporal duration of the launched transform-limited pulse will also increase the time duration of the SDW as this waveform must support the entire bandwidth of the optical pulse. In practice adding fiber length to increase system TBWP, adds measurable loss, but does not greatly affect processor volume, a distinct benefit over space domain approaches.

Over the last decade researchers have experimentally altered dispersion-induced SDWs to perform pulse shaping. The writing of spectral filters into CFBGs has been used to both generate and spectrally shape longitudinal SDWs [34-37]. The inability to reconfigure this type of grating with present technologies is a chief drawback. To circumvent this problem, an EO modulator driven by an arbitrary waveform can follow the source of chromatic dispersion to alter the dispersed temporal waveform [42] and perform time-domain spectral shaping (TDSS) [38]. However, while the spectral intensity of such an optical signal may be shaped, the possibility to directly create temporal features shorter than ~10 ps in the dispersed optical signal is impossible due to limits on modulation speeds. More recently, experimentally altering dispersion-induced SDWs to perform pulse shaping in a full Fourier synthesis pulse shaping approach has been described [12] and shown in mixed fiber-free space systems [13] and demonstrated in an all-fiber realization [14]. Within the last year, a practical variant of the synthesis method has been applied to communications for phase coding optical pulses in a coherent optical code-division multiple access scheme [27].

This chapter aims to provide a treatment of the generalized longitudinal spectral decomposition pulse shaping technique, while clarifying the impact of theoretical idealizations and the experimental practicalities of dispersion and electro-optic modulation. It is shown that chromatic dispersion provides a viable means for generation of SDWs of sub-picosecond pulses with application for pulse shaping. The distortions associated with higher order chromatic dispersion are also considered theoretically and experimentally for their degrading and beneficial effects. The chapter is arranged as such: Section 2.B contains analysis of the generalized dispersion-based pulse shaping technique. The nature of output pulses from such a system is explored and contrasted with the optical waveforms produced in traditional spatial-temporal pulse shaping schemes. An experimental demonstration and results are shown in Section 2.C while discussions are included in Section 2.D. Section 2.E, lastly, concludes.

2.2 Analysis

A general description of the fiber-based pulse shaping technique, shown in Fig. 2.1, includes propagation through a dispersive element, an EO modulator, and a conjugate dispersive element. Dispersed longitudinal SDWs following the SMF are described in the system using Eq. 1.7 where β_2 and β_3 terms are included. By applying a voltage signal *v(t)* to the modulator, the longitudinal SDW is filtered in time via the electro optic effect and the Mach-Zehnder structure of the modulator. The conjugate dispersive element, with flipped signs in the phase terms of Eq. 1.7, recomposes the optical signal and gives an output waveform with pulses at temporal shifts corresponding to all spectral components of *v(t)*. By the example modulation in Fig. 2.1, the output

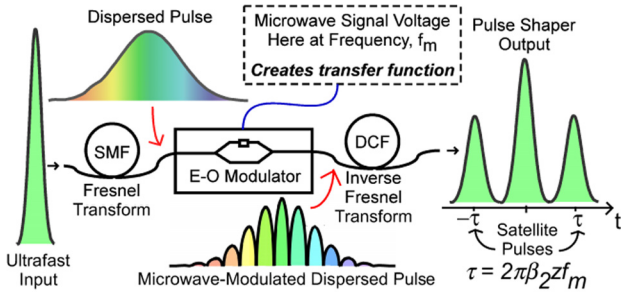

Fig. 2.1: General pulse shaping approach using dispersive fiber and an electro-optic modulator for signal processing.

waveform contains three pulses. The temporally displaced pulses generated from the AC components of *v(t)* are referred to here as satellite pulses but can be thought of as the microwave sidebands. A central pulse, corresponding to un-modulated optical signal, relates to the DC component of *v(t)*. In pulse shaping applications, *v(t)* is chosen to achieve general optical waveforms.

To first order the pulse shaping technique has advantageous properties when determining the maximum number of resolvable spots contained in generated optical waveforms. Due to the linearity of the system, temporal resolution is locked to the transform limited duration of the input pulse. However, by the nature of Fourier synthesis, long and detailed pulse shapes can be generated by creating fine spectral features. If the size of the point spread function in the spectral decomposition wave (SDW) is much smaller than the features of the filter, spectral feature size can be decreased in two ways. The size of a single element in the spectral filter can be decreased, or alternatively, the dimension of the SDW can be increased. In these directions spatial-temporal techniques are limited commonly by a finite spatial entrance pupil, grating resolution, and/or finite feature sizes in the spectral filters. The desire to increase the number of resolvable spots requires that these traditional pulse shaping

techniques grow in spatial dimension in order to achieve a large, high resolution SDW. The demands, incurred through expansion in spatial dimensions, on the complexity of the optical components eventually prove a hindrance to further improvement. In contrast to spatial processing techniques, the time aperture created by the longitudinal SDW of an optical pulse in a dispersive media grows longer simply with continued propagation. Furthermore, when increasing spectral resolution in this manner, the requirements on the spectral filter also prove advantageous. An EO modulator used to filter this SDW is immune to an increase in temporal dimension. In contrast, with a spatial processing approach (in the high resolution limit of the SDW) a spatial light modulator employed as a spectral filter must grow in transverse dimension to match an increased aperture. With the ability to create long duration SDWs and utilize high-speed modulators for spectral filtering, the dispersion-based pulse shaping technique has the potential for unprecedented time-bandwidth products.

A theoretical description of the pulse shaping technique begins in the frequency domain to facilitate inclusion of higher order dispersion terms using transfer functions. An analogous time-domain description, not including distortions, can be found in Ref. 15. While all terms from the expansion of $\beta(\omega)$ will have an effect on the dispersion-based pulse shaping technique, experimentally β_2 and β_3 (the second and third orders) prove most important. The former provides the linear separation of spectral components necessary for SDW generation while the latter acts as the strongest system distortion (i.e. aberration). Our analysis and implementation center on the use of optical fibers as the source of chromatic dispersion due to widespread availability. CFBGs are also considered theoretically for their controllable dispersion characteristics. Optical

nonlinearities can be discounted in dispersion compensated links for sub-picosecond pulses provided optical powers are maintained at levels that do not lead to self phase modulation (SPM) [52]. SPM, when present, degrades the ability to recompress the optical pulse as will be seen in the next sections. For analysis, all passive elements in the system are treated as linear and time-invariant. Moreover, as we make use of the slowly varying envelope approximation (SVEA), our analysis is valid only for launched pulses greater than ~100 fs [53].

Consider a sub-picosecond transform limited pulse at $z = 0$ with its spectrum $U(0,\omega)$ propagating along the *z*-axis. After the first SMF span, a dispersion induced SDW is described by Eq. (1.7). Modulating the dispersed waveform with ideal signal $v(t)$ and then propagating through a dispersion compensating element providing standard dispersion, described by a propagation constant, $\beta'(\omega)$, and length, z', leads to an output waveform in the frequency domain,

$$U_{\text{out}}(z,\omega) = \left(\int_{-\infty}^{\infty} V(\omega-\omega')U(0,\omega') \exp\left[-j\frac{1}{2}\beta_2 z(\omega')^2 - j\frac{1}{6}\beta_3 z(\omega')^3 \right] d\omega' \right) \times \exp\left[-j\frac{1}{2}\beta_2' z'\omega^2 - j\frac{1}{6}\beta_3' z'\omega^3 \right] \quad . \quad (2.1)$$

Here we used the fact that multiplication of the SDW in the time-domain by $v(t)$, corresponds to convolution in the frequency domain between $V(\omega)$ and the SDW of Eq. (1.7). When making the Fraunhofer approximation, the filtering signal, $v(t)$, can be expressed as modulating the spectrum of the optical pulse directly; analogous to the

operation of spatial light modulators in traditional spatial-temporal pulse shapers. However, for accuracy in our model, modulation is restricted to the time-domain, and the spectrum of $v(t)$ is convolved with the spectrum of the chirped pulse.

Matching dispersive elements for complete compensation of second and third order dispersion is possible but necessitates extreme care. When only second order dispersion is considered, we must strive to balance all propagation lengths to precise tolerances. A trial and error approach with varying the lengths of the two media can succeed to exactly match the magnitudes of $\beta_2 z$ and $\beta'_2 z'$ However, when third order dispersion is considered, we rely on the dispersive device manufacturers to appropriately create the dispersion and dispersion slope of each element. If $\beta_3 z$ is to simultaneously match $\beta'_3 z'$ when second order dispersion is compensated, the ratio of β_2 to β'_2 must exactly equal the ratio of β_3 to β'_3. Optical fiber manufacturers developed dispersion compensating fibers (DCFs) that are matched to their single mode fiber (SMF) products, prompting an initial assumption that complete dispersion compensation of both β_2 and β_3 is fair. Presuming the two dispersive elements are exactly matched, the second dispersive element contributes quadratic and cubic phases identical to those of the first but opposite in their signs. Therefore $\beta'_2 z'$ and $\beta'_3 z'$ are equal to $\beta_2 z$ and $\beta_3 z$ in magnitude respectively. For simplicity of notation both quadratic phase terms will have strength $\beta_2 z$ while the first, carried from Eq. (1.7), will be set positive (i.e. β_2 is negative) to represent propagation in the anomalous dispersion regime. The second, entering in Eq. (2.1), will remain negative for standard dispersion. For the cubic phase

terms $\beta'_3 z'$ is set equal to negative $\beta_3 z$ following the scenario in commercial SMF and DCF fibers.

Examining a sample modulation signal helps to understand the physical meaning of Eq. (2.1). If the modulator provides a microwave signal with DC and components at fundamental frequency, ω_o, then $V(\Omega) = A\delta(\Omega) + B\delta(\Omega - \omega_0) + B\delta(\Omega + \omega_0)$. Note that we assume the period, $2\pi/\omega_0$, to be shorter than the time aperture created by the SDW. Inserting the signal, $V(\omega)$, into Eq. (2.1), performing the convolution, expanding the exponentials, and multiplying the dispersion compensation phase terms through leads to

$$\begin{aligned} U_{\text{out}}(z,\omega) = AU(z,\omega) &+ \left\{ BU(z,\omega-\omega_o)\exp\left[j\frac{1}{6}\left(3\beta_2 z + \beta_3 z\omega_o\right)\omega_o^{\,2}\right]\right. \\ &\left.\times\exp\left[-j\left(\beta_2 z + \frac{1}{2}\beta_3 z\omega_o\right)\omega_o\omega\right]\exp\left(j\frac{1}{2}\beta_3 z\omega_o\omega^2\right)\right\} \\ &+ \left\{ BU(z,\omega+\omega_o)\exp\left[j\frac{1}{6}\left(3\beta_2 z - \beta_3 z\omega_o\right)\omega_o^{\,2}\right]\right. \\ &\left.\times\exp\left[j\left(\beta_2 z - \frac{1}{2}\beta_3 z\omega_o\right)\omega_o\omega\right]\exp\left(-j\frac{1}{2}\beta_3 z\omega_o\omega^2\right)\right\} \end{aligned} \quad . \qquad (2.2)$$

The three copies of the original pulse spectrum correspond to the frequency make-up of the modulating signal *v(t)*, i.e. the DC signal and sidebands respectively. The linear phase affecting the two frequency shifted pulses signifies the temporal advancement and delay of these satellite pulses. However, we observe that the original transform limited pulse waveform is obtained only for the first copy of the pulse spectrum in Eq. (2.2),

whereas a quadratic phase modulates the other two. This quadratic spectral phase will chirp and broaden the satellite pulses in the same way chromatic dispersion operates, and most importantly, its strength is proportional to the frequency of modulation. Performing an IFT on Eq. (2.2) provides a time-domain output for the system. The operation is simplified by transforming the pulse, constant phase and linear phase together, independently from the quadratic spectral phase. In the time-domain, the transforms are rejoined by a convolution integral represented by the operator $\otimes$ as follows

$$\begin{aligned} U_{\text{out}}(z,t) = AU(z,t)\exp\left(j\omega_c t\right) + \left\{ B\exp\left[-j\left(\frac{1}{2}\beta_2 z + \frac{1}{3}\beta_3 z\omega_o \right)\omega_o{}^2 \right]\exp\left[j(\omega_c + \omega_o)t \right] \right. \\ \left. \times U(z, t - \beta_2 z\omega_o - \frac{1}{2}\beta_3 z\omega_o{}^2) \otimes \exp\left(-j\frac{t^2}{2\beta_3 z\omega_o} \right) \right\} \\ + \left\{ B\exp\left[-j\left(\frac{1}{2}\beta_2 z - \frac{1}{3}\beta_3 z\omega_o \right)\omega_o{}^2 \right]\exp\left[j(\omega_c - \omega_o)t \right] \right. \\ \left. \times U(z, t + \beta_2 z\omega_o - \frac{1}{2}\beta_3 z\omega_o{}^2) \otimes \exp\left(j\frac{t^2}{2\beta_3 z\omega_o} \right) \right\} \end{aligned} \quad . \quad (2.3)$$

The first term, representing the DC signal, is both transform limited and free of a temporal shift. The two satellite pulses, representing the sidebands, are shifted temporally from the central position on the time axis. The temporal shifts of $\pm\beta_2 z\omega_0$ are the desired result of the pulse shaping procedure. However, the presence of third order dispersion provides a secondary temporal shift that, although small, must be considered for signal processing. More detrimental to pulse shaping is the convolution of the satellite pulses with a quadratic phase, which leads to temporal broadening and a

respective decrease in their peak power. Because the amount of temporal broadening is directly proportional to the microwave carrier frequency ω_o, satellite pulses temporally shifted farther from the central pulse will see larger temporal expansion. Ultimately, large temporal shifts will lead to a lack of temporal confinement and peak power that may prove inadequate for pulse shaping applications and detection systems. This physical result has a space-domain analog. It is known that spatially filtering the spatially-dispersed spectrum of a signal in free space leads to chirped satellite pulses.

To better understand the effect of higher order dispersion on the pulse shaper, it helps to consider again the operating principle. The processor creates delayed copies of the original pulse through frequency shifting the signal at the last pre-compensation point of a dispersion-compensated link. While the technique is introduced in this section for ultrafast optical waveform synthesis, the general approach is receiving attention as a method for "slow-light" optical buffering of longer, optical communication pulses [28,29,54]. This community likes to refer to frequency shifters (the EO modulators) as time prisms. Recall that the principle of operation is to introduce a variable group delay through upshifting or downshifting the carrier frequency before the compensating fiber, where β_2 gives the desired group velocity adjustment to the frequency shifted signal. Similarly, if β_3 is present, it results in a group velocity dispersion adjustment. Thus time delayed/advanced pulses will see residual uncompensated group velocity dispersion, which causes pulse broadening.

As an aide for potential users, a figure of merit for the system is defined as the temporal shift, T_D, of a satellite pulse that results in a doubling of pulse duration. If the pulses are assumed Gaussian, the quadratic phase resulting from β_3 broadens the satellite

pulses as $T_1 = T_0\left[1+\left(\beta_3 z\omega_0/T_0^2\right)^2\right]^{1/2}$, where T_0 and T_1 are the transform-limited and broadened half-widths at 1/e-intensity point [53]. The temporal shift of each satellite pulse is $T_S = \beta_2 z\omega_0$, if the small shift due to β_3 is ignored. Thus we determine that when $T_1/T_0 = 2$, $T_S = T_D = \sqrt{3}\,T_0^2\beta_2/\beta_3$. For a system employing commercial communication fiber with β_2≈-20 ps^2/km and β_3≈0.1 ps^3/km and a laser source producing pulses with T_0≈0.1 ps, T_D is roughly 4 ps. It should be noted that if β_3 is reduced relative to β_2, the broadening of satellite pulses becomes less severe as is reflected in the equation for T_D. Third order dispersion then introduces a trade-off between design simplicity (use of commercial, off-the-shelf fibers) and performance (limited number of resolvable spots and TBWP).

While for some applications, shaped waveforms of limited temporal duration (~10 ps) may not be a problem, high speed signal processing applications demand an alternative approach, which realizes large TBWPs. Use of CFBGs with tailored dispersion can result in a system without higher order dispersion terms. If a solution to the birefringence issue were uncovered, a CFBG could be employed in the fiber-integrated system to set β_3 and higher order terms to near-zero. For such a system a Fourier transform of Eq. (2.2) is written as:

$$U_{\text{out}}(z,t) = AU(0,t)\exp(j\omega_c t) + B\exp\left[-j\frac{1}{2}\beta_2 z\omega_0{}^2\right]U(0,t-\beta_2 z\omega_0)\exp\left[j(\omega_c+\omega_0)t\right] + B\exp\left[-j\frac{1}{2}\beta_2 z\omega_0{}^2\right]U(0,t+\beta_2 z\omega_0)\exp\left[j(\omega_c-\omega_0)t\right] \quad . \quad (2.4)$$

Here the temporal shifts of the satellite pulses are proportional to the strength of β_2 only, and the quadratic phase broadening the satellite pulses is gone. Again the constant phase in Eq. (2.4) modulating the two sidebands is present but can be ignored. Due to "far-field" propagation, this phase term results in negligible phase offsets between overlapping satellite pulses. A linear phase term modulating each satellite pulse in Eq. (2.4) remains from Eq. (2.3) and cannot be dismissed. These linear phases are seen to upshift and downshift the temporal bandwidth of the delayed and advanced pulses, respectively, by the modulation frequency. With the use of an EO modulator for signal filtration, these "Doppler shifts" may approach tens of GHz. While frequency shifts from the carrier are present in the satellite pulses created in traditional pulse shaping methods as well, such shifts are smaller because slower modulators are utilized. To reduce the frequency shifts of the satellite pulses in our technique, a larger dispersion-induced time aperture is needed. As seen in Eqs. (2.3) and (2.4), temporal shifts of the satellite pulses are proportional to $\beta_2 z \omega_0$. Thus for a given time shift, ω_o can be decreased if z is increased. The coupling of time and frequency is a characteristic feature of the dispersive pulse shaping system due largely to the nature of the approximate Fourier transform performed by propagation in a dispersive medium. While the Doppler shift is removed under the "far-field approximation" (where all phase terms in Eq. (2.4) are set to one), it truly becomes insignificant only with extremely large time apertures and slow modulations speeds. Though not critical to all pulse shaping applications, this dependence of frequency shifts on temporal shifts need be considered when performing signal processing.

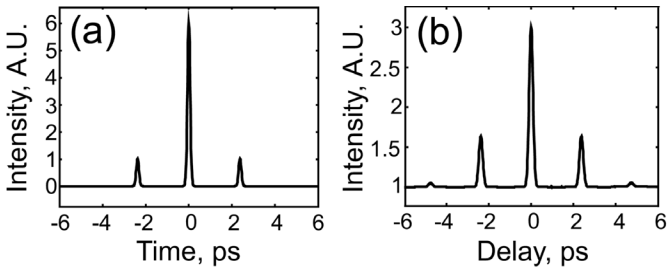

Fig. 2.2. (a) Modeled intensity of a temporal waveform output from the system as described by Eq. (2.4). Time is designated relative to the central pulse that corresponds to the constant (DC) component of the modulating signal *v(t)*. The satellite pulses relate to the microwave sidebands, ±7 GHz. Here the microwave signal is weaker than the DC. (b) Intensity autocorrelation trace (with background) of the modeled optical waveform in (a). The small pulses occurring at ±4.7 ps are cross correlations of the pulses at ±2.3 ps in (a). The cross correlation of the DC and satellite pulses in (a) form the pulses at ±2.3ps in (b).

The intensity waveform resulting from a simulation that follows the model developed by Eq. (2.4) is shown in Fig. 2.2(a). The modulating signal is identical to the *v(t)* used in Eq. (2.2) where the coefficients are such that the DC component is stronger than the microwave signal ($A>B$). The launched 150 fs pulse was stretched to and compressed from a nanosecond with purely second order dispersion, and the modulating tone is set such that ω_0 is equal to $2\pi\cdot 7$ Grad/s. Satellite pulses should appear at temporal locations $t=\pm\beta_2 z\omega_0$, which correspond to roughly ±2.3ps as $\beta_2 z=52$ ps^2. As a validation of the concept, it is apparent that the ratio of the temporal shift of the side pulses to the temporal width of the launched/recompressed pulse roughly equates with the ratio of the time window created by the dispersed pulse to the period of the modulating signal. Due to the difficulties in measuring optical waveforms with sub-picosecond features, Fig. 2.2(b) shows the results of a practical solution to detection: an intensity autocorrelation (with background) of the signal in Fig. 2.2(a). For microwave spectrum analysis applications as described in Chapter 3, one can determine the microwave spectral content

of an unknown signal $v(t)$ by examining the temporal waveform output from the system while scaling time to frequency by $t/\beta_2 z=\omega$. Eq. (2.4) here provides an identical result to the time-domain analysis performed in Ref. 15 if $v(t)$ from this example is inserted into Eq. (4) of Ref. 15, and the convolution is carried out there. For general pulse shaping applications, desired pulse shapes are created through the control of the modulating signal, $v(t)$.

In a complete description of the pulse shaping process, the details of the modulation scheme must be considered. It is apparent that the longitudinal SDW creates a time aperture over which the modulation signal is windowed. In order for a spectral component of $v(t)$ to create a satellite pulse distinguishable from the DC pulse at the system output, its period must be shorter than the time aperture. Because the time aperture of a longitudinal SDW cannot temporally overlap the SDW from the following or preceding pulse in the train, the repetition rate of the laser system places an upper limit on dispersive propagation length, time aperture duration, and the period of $v(t)$. The shortest temporal feature in the shaped waveform, however, is limited by the optical bandwidth. Regarding the maximization of temporal shifts for satellite pulse (e.g. TBWP or number of resolvable spots), higher order dispersion introduces the most stringent confinement. When this effect is removed or disregarded, as in Eq. (2.4), modulator speed becomes the principle limit. The largest temporal shifts ($T_S=\beta_2 z\omega_0$) occur when both the speed of the modulator (ω_0) and duration of the SDW time aperture ($\sim\beta_2 z$) are maximized. Of additional importance to SDW modulation is the nature of the EO modulator itself. As was revealed in Chapter 1 and reinforced through the analytic treatment of this section, the frequency shifts associated with temporal modulation result

in temporal shifts of the longitudinal SDW. Anticipating pulse shaping results from a longitudinal pulse shaping system requires a definition of the relationship between the frequency content of the SDW modulation and that of the microwave driving signal. Practically, the spectrum of the modulation applied to the dispersed optical field, represented in Eq. (2.1) as $V(\omega)$, depends not only on the applied microwave/RF signal, but also upon the characteristics of this modulator. Mach-Zehnder devices commonly used for intensity modulation in optical communications are well understood, and a mathematical treatment is reserved for Appendix 2-A. An important detail is that the pulse shaping technique utilizes field modulation and not intensity modulation. Null biasing a standard communications modulator allows for linear application of a desired microwave signal to the optical field of the longitudinal SDW, provided that the applied voltages do not approach a large fraction of V_π for the modulator. Under these conditions the bias and signal amplitudes applied to the EO modulator control the coefficients A and B in Eqs. (2.3) and (2.4).

2.3 Experimental System and Results

The experimental approach to realize pulse shaping is shown schematically in Fig. 2.3. A Coherent MIRA Titanium Sapphire laser pumps optical parametric oscillator (OPO) delivering 150 fs transform limited pulses at 76 MHz and a nano-Joule of energy per pulse. The matched dispersive elements are spools of SMF and a DCF module. The operating wavelength is tuned to 1.55 μm to minimize attenuation and realize substantial dispersion. A grating stretcher and attenuator precede coupling into the SMF to avoid optical nonlinear effects associated with the highest peak intensities. Approximately 2.6

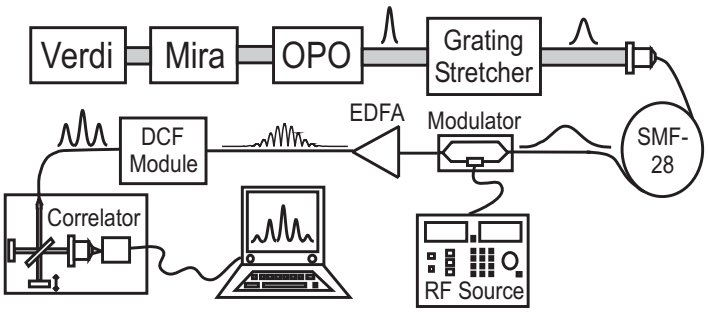

Fig. 2.3: Experimental setup for realization of sub-picosecond pulse shaping.

km of SMF are employed to disperse the pulse to a nanosecond full width at half maximum (FWHM). That the dispersed and launched pulses have identical spectra, when the former is scaled to remove attenuation, confirms the dominance of dispersion over SPM in the SMF. Specifically for our launch conditions, the ratio of the dispersion length to the nonlinear length, sometimes denoted as the soliton number, equals $N^2 \approx .035$ [53]. Dispersion compensation occurs in a DCF module providing -44 ps/nm. In the linear propagation regime the order of the two fiber types is arbitrary. However, it is worth noting that soliton propagation is not supported in DCF and power levels necessary to induce SPM are higher in DCF than in SMF. Therefore, for operation close to the nonlinear threshold (i.e. where $N^2 > .1$) the system should proceed with DCF. Operation with pulse energies above a nano-Joule is possible using significant pre-stretching and post-stretching to lower peak powers below SPM inducing levels. Experimentally, launching pulses on the order of 100 femtoseconds requires that all fibers/pre-chirping devices be matched with high precision. The length of SMF must be tailored to within a few meters of the ideal length to measure a sub-picosecond pulse at the output. Spectral filtering via modulation is performed by a 10 GB/s $LiNbO_3$ Mach-Zehnder intensity modulator. The swept frequency source used to drive the modulator with single

sinusoidal waveforms delivers electrical powers less than 24 dBm. An erbium-doped fiber amplifier (EDFA) follows the modulator to boost signal strength. Note that the erbium fiber provides standard dispersion and must be factored in when determining the amount of SMF required. The output waveform from the DCF is measured using a Michelson interferometer-based autocorrelator. To view the interferometric autocorrelation trace (ACT), an amplified silicon photodiode is operated in a nonlinear detection mode via two photon absorption (TPA) [55]. The TPA detection scheme provides useful phase sensitivity that gives experimental verification of full pulse recompression after propagation in the DCF. The nonlinear detection also facilitates detection of the time/frequency shifted satellite pulses since the cross correlation of these pulses (within the autocorrelation of the entire waveform) will average to the background level with a slow linear detector. The intensity requirements of the TPA process, however, require that the EDFA be used in the system. If the system were not driving a nonlinear process, the EDFA could be omitted.

Detected results from the experimental setup described above are given in Fig. 2.4. The two intensity autocorrelations are generated through digital post processing of measured interferometric ACTs. In both cases the RF signal generator supplied a 7 GHz sinusoid with 15 dBm electrical power. In the experiments represented in Fig. 2.4(a) the bias to the modulator is controlled such that a strong DC (un-modulated) component is allowed to pass. Relating to Eqs. (2.3) and (2.4), the optical field can be described with coefficient A greater than coefficient B. The temporal shift, $T_S = \pm\beta_2 z\omega_0$, should correspond to ±2.3ps. Correspondingly Fig. 2.4(a) shows close similarity to the modeling output of Fig. 2.2(b). Here again the small pulses at ±4.7 ps in the ACT are formed by

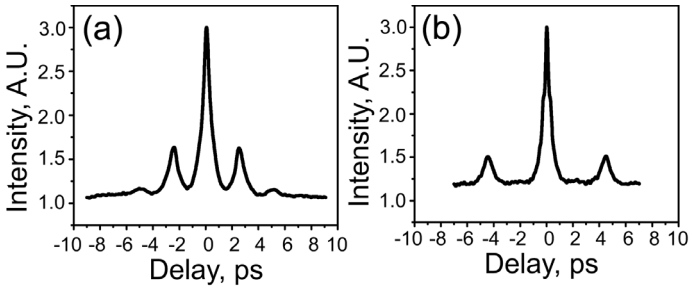

Fig. 2.4: Experimental intensity autocorrelation traces of signals with 7 GHz modulation. RF power is maintained at 15dBm while bias voltage is varied. (a) ACT in the presence of a strong DC component in the modulating signal v(t). Experimental result shows agreement with the trace obtained from our linear model in Fig. 2.2(b). (b) ACT when the modulator was null biased. The autocorrelation process leads to the formation of three pulses as the inner two satellite pulses drop out.

the cross correlation of satellite pulses at ±2.3 ps in the output optical waveform. The strong central pulse in the output field cross correlating with a satellite pulse leads to the pulses at ±2.3 ps in the ACT. In Fig. 2.4(b) the modulator is null biased to completely remove the un-modulated component. The output field is described by setting A to zero in Eq. (2.3). Confirmation of carrier suppression is given by the complete removal of visible pulses at ±2.3 ps in the detected intensity ACT. The elevation of the signal background in Fig. 2.4(b) from 1 to just less than 1.2 is evidence of an uncompressed background arising from SPM and dispersion. The background is estimated to contain approximately 75% as much power as the signal. Here the localized loss of the null biased modulator led to a compensating increase of power above the nonlinear threshold at another location in the system. This background is undesirable and can be avoided, as seen in Fig 2.4(a), with stricter power budgeting and avoidance of nonlinear interactions.

As stated, the choice of optical fiber as the low-loss dispersion element in our experimental setup stems from its widespread availability. However, a number of factors

limit the ability of optical fiber to provide a true SDW. Both optical nonlinearities and higher order dispersion terms can contribute to the degradation of the signal in a fiber-based implementation of the temporal pulse shaper. While combating nonlinear effects is possible if high peak powers are avoided, the third order dispersion of silica fiber must be considered. Thus, in practice, the complexities and drawbacks expressed in Eq. (2.3), as opposed to the simple description of Eq. (2.4), need be used to describe the pulse shaping system.

The experimental results confirming the presence of the temporal broadening with increased modulation frequency, ω_0, as predicted in Eq. (2.3) are shown in Fig. 2.5. The EO modulator was again null biased to minimize the un-modulated component passing the modulator. The optical field following the dispersion compensation module contained two recompressed pulses, representing the up and down shifted components.

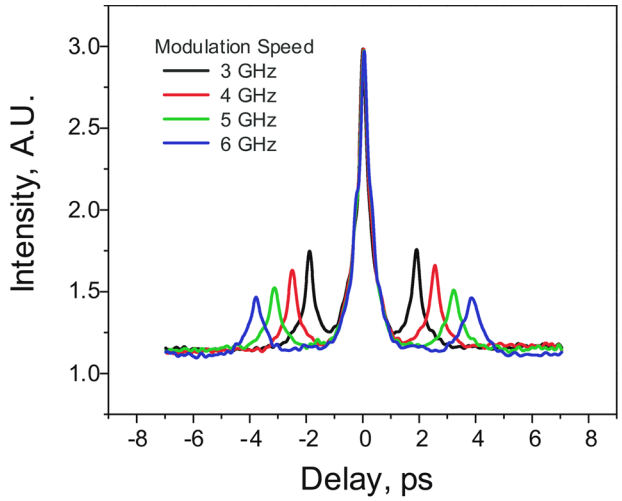

Fig. 2.5: Overlaid intensity autocorrelations showing the effect of increased modulation frequency on pulse shaped waveform. The temporal broadening of the 6 GHz up and down shifted pulses is apparent when comparing their FWHM to those pulses originating from 3 GHz modulation.

With three pulses in each overlaid ACT in Fig. 2.5, the advanced and delayed correlation pulses represent the cross correlation of the two pulses constituting the optical field. Visually comparing the FWHM of the advanced and delayed pulses corresponding to the 6 GHz modulation with those corresponding to the 3 GHz modulation clearly shows the broadening described theoretically. An increase of the signal background is again attributed to the increased signal strength needed to overcome the point loss at the null biased modulator.

2.4 Discussion

Examining experimental results in Fig. 2.5 leads to a better understanding of the roles of β_2 and β_3 and the importance of their proper compensation. The results shown in Fig. 2.5 depart somewhat from those predicted for an autocorrelation of the field expressed in Eq. (2.3) (where $A<<B$). Each of the normalized curves in the overlaid intensity correlation traces is clearly not formed by a sequence of two pulses equal in FWHM duration. Such a field, when correlated, should always form a central pulse of twice the height and similar width to the outer pulses in the trace. Furthermore, despite the increase in pulse duration with larger temporal shifts for the side pulses in the figure, the central pulse remains markedly constant in width. The pulse triplets in the overlain ACTs of Fig. 2.5 must arise from optical signals containing two pulses of different peak intensities and durations. To better understand these optical fields that gave rise to the ACTs in Fig. 2.5, it is useful to reexamine the theoretical description of the distorted system described by Eqs. (2.2) and (2.3). The equations show that while the length of SMF and DCF can be set to produce only one transform limited pulse at the output, this

pulse need not be the central "DC" pulse. Adding the effect of residual second order dispersion at the output of the DCF with the quadratic phase generated for up and down shifted pulses due to β_3, a delayed or advanced pulse can be made to be nearly transform-limited. In a system with exact β_3 cancellation, a small amount of second order dispersion added to the field spectrum in Eq. (3) can cancel the term $\exp\left(\pm j \frac{1}{2} \beta_3 z \omega_0 \omega^2\right)$ for a single satellite pulse. As an example the residual quadratic phase given for an extra half meter of SMF is nearly identical in magnitude to the quadratic phase resulting from β_3 for a 5 GHz shifted pulse in the experimental system described above. In such a scenario the advanced pulse in the output waveform is transform limited, while the delayed copy is twice as broad as it would be with exact β_2 cancellation. In general, using additional second-order dispersion to cancel the quadratic phase from β_3 leads to an advanced and delayed satellite pulse pair with a differential in amplitude and spreading that relates to the strength of β_3 and their distance from the central "DC" point. A small additional cubic phase is inevitable and would need to be practically considered. However, the idea lends itself to envisioning a system employing an adjustable dispersive element following the DCF designed to permit the user to select a satellite pulse from the output waveform to compensate and make transform limited. Examples of such dispersive devices are a free-space grating stretcher or as a more complex alternative, a traditional free space pulse shaper. For a microwave spectrum analysis technique, an operator could sweep across a spectral zone of interest maximizing resolution at each point of observation. While for pulse shaping, the interplay of second and third order dispersion lends itself to the creation of asymmetric waveforms.

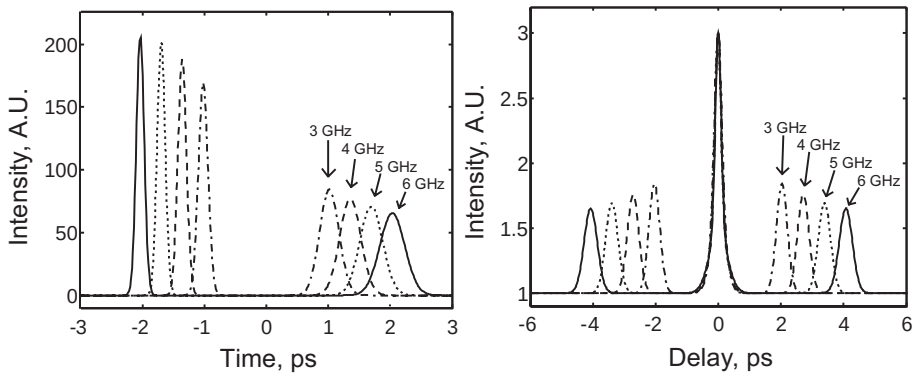

Fig. 6: Modeling results of pulse shaping in the combined presence of β_3 and residual second order chromatic dispersion. (Left) Intensity traces showing the asymmetric pulse duos created for four modulation frequencies. For a system with 60 centimeters extra SMF (out of 2.6 km) the trailing pulses in the pairs are broadened significantly as compared to the lead pulses. (Right) Intensity ACTs of the intensity waveforms at left. The ACT results on the right show agreement with the experimental data displayed in Fig. 2.5.

A confirmation of the theoretical description and experimental results is given in Fig. 2.6. The model used to produce the results of Figs. 2.2 and 2.4(a) is expanded to include the cubic spectral phases originating in SMF and DCF. To negate additional pulse features the cubic phases were set to balance precisely while the quadratic phases included a mismatch corresponding to 60 additional centimeters of SMF. Fig. 2.6(left) shows the optical intensity after the DCF where the asymmetry of the pulsed waveforms is clearly visible for all frequencies of modulation. The temporally advanced pulse in all four cases is shown to be much closer to a transform limited state than the delayed pulse. A set of overlaid intensity autocorrelations of the modeled fields from Fig. 2.6(left) comprise Fig. 2.6(right). The result shows good agreement with the detected shape and microwave frequency dependence of Fig. 2.5. Due to the symmetry of the ACT, the intensity waveforms of Fig. 2.6(left) are not a unique solution to Fig 2.6(right). A system lacking 60 centimeters of DCF would show an imbalance similar to Fig. 2.6(left) but with

the temporally delayed pulse compressed relative to the leading pulse. The resulting ACTs would be identical. As such, we rely on our knowledge that the waveforms in Fig. 2.5 were formed by a system imbalanced by additional SMF.

In practice manufacturing DCF to cancel both second and third order dispersion to the tolerances demanded by sub-picosecond pulses most often does not occur. The assumption of complete compensation of the cubic phase from the SMF by the DCF that allows Eq. (2.2) to be written is generally inaccurate. The ratio of β_{2_SMF} to β_{2_DCF} will vary slightly from the ratio of β_{3_SMF} to β_{3_DCF}. Two DCFs with differing dispersion parameters can be used in concatenation to completely cancel both β_{2_SMF} and β_{3_SMF} [56]. However, when the experimental system is designed with a single DCF type to exactly cancel second order dispersion, the likely result is a small residual cubic phase term in Eq. (2.2) for all pulses in the output waveform. In the time-domain each individual pulse comprising the larger waveform will take on an asymmetric shape. Due to the nature of the autocorrelation detection scheme, such pulse asymmetry is lost in the measured ACTs of Figs. 2.4 and 2.5. As discussed an alternative experimental setup using a single DCF would achieve exact β_3 cancellation. The residual second order dispersion could be removed with an additional dispersive element or be used to cancel the quadratic spectral phase originating from β_3 for a satellite pulse.

2.5 Summary and Acknowledgement

This chapter demonstrates an approach to sub-picosecond pulse shaping in a fiber-based arrangement using longitudinal spectral decomposition. Experimental results are presented and show strong agreement with the model developed. The ability to

faithfully reproduce detected autocorrelation traces with simulations supports the validity of the linear system model. Examination of these results confirms the functionality of the dispersion-based pulse shaper while giving insight into the issues surrounding third-order chromatic dispersion as a distortion in the system. Making use of commercially available telecom fiber and instruments, the technique is highly suitable for integration with current communications systems. Confinement to a single mode fiber removes the time/space interrelation inherent in traditional pulse shaping devices, and it allows one to envision pulse shaping during propagation over long dispersion compensated spans. The concept lends itself to new signaling methods including in-line schemes for coherent optical code division multiple access (OCDMA), for which recent initial demonstrations were made [27]. For signal processing applications requiring large TBWPs, higher-order dispersion is exposed as both a limitation to the temporal extent of generated waveforms and an advantage for creating asymmetric pulse shapes. The use of CFBGs as a fiber integrated source of chromatic dispersion was theoretically presented as a method for creating a distortion-free system. Ultimately, the CFBG method could realize the potential advantage of our dispersion-based technique over conventional time-space approaches for achieving large TBWPs. Dispersing the SDW to durations approaching a 100 ns time window and utilizing modulating devices in the tens of GHz range, more than 10^4 resolvable spots is conceivable with shaped waveforms lasting over a nanosecond. Alternative sources of modulation could be employed to replace the asymmetry in produced waveforms previously delivered by third-order chromatic dispersion. Electro optic phase modulators and slower AO modulators offer single sideband modulation resulting in satellite pulse generation on one side of the central point. The coupling of

frequency and time shifts in the dispersion-based pulse shaping system is a fundamental characteristic that must be factored in when large time shifts are needed and actual applications are considered.

The text of Chapter Two, in part, is a reprint of the material as it appears in:

R.E. Saperstein, N. Alic, D. Panasenko, R. Rokitski, Y. Fainman, "Time-Domain Optical Processing using Chromatic Dispersion for Ultrashort Pulse Shaping," J. Opt. Soc. America B 22, 2247-2436 (2005).

The dissertation author was the primary researcher and author. The co-authors listed in this publication directed and supervised the research that forms the basis for this chapter.

APPENDIX 2-A

In this appendix transmission characteristics of the EO modulator used to modulate the optical SDW field are discussed. Due to its Mach-Zehnder structure, the device retains a sinusoidal transmission characteristic versus applied voltage. However because the optical field is of concern in the pulse shaping technique, the transmission relationship has twice the period when compared to a traditional intensity modulation scheme, thus yielding

$$t_{field}(v) = \cos\left[\frac{\phi_o}{2} + \frac{\pi v(t)}{2V_\pi}\right]. \tag{2.5}$$

Here ϕ_o is the optical path length difference of the two arms of the interferometer, while *v(t)* represents the signal voltage, and V_π is a voltage specification for the modulator. The signal voltage is in general $v(t) = V_b + V_m \sin(2\pi f_m t)$ where V_b is the bias voltage, V_m is

the modulation amplitude, and f_m is the frequency of modulation. Inserting the signal voltage, Eq. (2.5) expands to:

$$t_{field}(V_b, V_m, f_m, t) = \cos\left(\frac{\phi_o}{2} + \frac{\pi V_b}{2V_\pi}\right)\cos\left(\frac{\pi V_m}{2V_\pi}\sin(2\pi f_m t)\right) - \sin\left(\frac{\phi_o}{2} + \frac{\pi V_b}{2V_\pi}\right)\sin\left(\frac{\pi V_m}{2V_\pi}\sin(2\pi f_m t)\right) \quad . \tag{2.6}$$

It is clear that the bias voltage plays an integral role in determining the comparative strength of the two terms. By appropriately selecting the bias voltage with knowledge of ϕ_o, the transmission of the field through the modulator will depend on a cosine of the applied signal voltage, a sine of the applied signal voltage, or a relative combination of each. To obtain a more meaningful view of this implication, a Fourier series expansion of the two terms gives

$$t_{field}(V_b, V_m, f_m, t) = \cos\left(\frac{\phi_o}{2} + \frac{\pi V_b}{2V_\pi}\right)\left[J_0\left(\frac{\pi V_m}{2V_\pi}\right) + \sum_{\substack{n=2 \\ n,even}}^{\infty} 2J_n\left(\frac{\pi V_m}{2V_\pi}\right)\sin(2\pi n f_m t)\right] - \sin\left(\frac{\phi_o}{2} + \frac{\pi V_b}{2V_\pi}\right)\left[\sum_{\substack{n=1 \\ n,odd}}^{\infty} 2J_n\left(\frac{\pi V_m}{2V_\pi}\right)\sin(2\pi n f_m t)\right] \quad . \tag{2.7}$$

Here $J_n(\ )$ represent an n-th order Bessel function of the first kind. Inspecting Eq. (2.7) it is clear that the SDW is modulated by not only the applied signal voltage but also a weighted collection of the entire set of harmonics. The bias voltage plays the role of selecting whether the odd harmonics, even harmonics (and DC), or both are represented

in the modulation. The amplitude of the signal voltage, V_m, further determines the relative coefficient of each harmonic. Thus, for pulse shaping applications two degrees of freedom are present in controlling the outcome of the experiment when employing such a Mach-Zehnder device. Following the descriptions given by Eqs. (2.3) and (2.4), the bias and signal amplitude are used to control the relative strength of the coefficients A and B. While null-biased, the modulator experimentally used offers an extinction ratio of ~19dB for a 15dBm driving voltage. This level of carrier suppression justifies setting the A coefficient to zero when desired, and demonstrates the ability to extinguish the even harmonics. Ultimately, because the spectral components of the modulating signal manifest themselves as pulses at the output of the pulse shaper, controlling the bias and amplitude allows for creation of a pulse sequence of varying heights and spacing with application of a single microwave tone. Limitation to the height of a satellite pulse comes from the Bessel function expansion, which necessitates the creation of higher harmonics at large driving voltages. Fig. 2 of Ref. 15 shows clear signs of higher harmonics in the detected ACT stemming from a 23 dBm driving voltage. As an important experimental note, appropriate selection of the electronic signal parameters allows for working around frequency limitations of the modulator or signal generator to achieve larger pulse separations without adding more matched fiber (i.e. without increasing z in Eq. (2.3)).

Chapter 3

Microwave Photonics with Longitudinal Spectral Decomposition Processing

3.1 Introduction

The processing of radio frequency (RF), microwave, and millimeter wave signals with optics is a well established field of scientific study [57]. A majority of the current efforts on topic are aimed at transporting radio- and micro-wave signals over fiber networks for signal distribution and true-time delay realization. A smaller sub-section of microwave-photonic research looks to exploit the large optical carrier frequency to generate or detect slower microwave speed signals [15-19, 58]. Longitudinal SDWs formed from ultrashort pulses are uniquely suited to contribute to this sub-field. The large total optical bandwidth, exceeding several THz, implies great processing power while the narrow instantaneous frequency-swept optical carrier linewidth, below 100 MHz, permits high signal processing precision. In this chapter, a specific processing system for longitudinal SDWs is introduced and shown applicable to both microwave spectrum analysis and microwave signal generation.

To bridge the enormous frequency gap between optics and microwaves, narrowband difference-frequency signals are generated through the interference of multiple longitudinal SDW copies under delay [59]. This coherent processing step is used throughout this and the next chapter to create intermediate frequencies (IF) in the radio and microwave region. A theoretical description of the process proceeds by first assuming longitudinal SDW generation in an ideal dispersion source with no higher order terms. Eq. (1.6) is simplified by replacing $U_1(0,\omega')$ with the pulse $U(0,\omega')$ that has no higher order phases, giving a temporal SDW

$$u(z,t') = h_0 \exp\left(j\frac{t'^2}{2\beta_2 z} \right) U(0,\omega')\Big|_{\omega'=t'/\beta_2 z}. \tag{3.1}$$

From Eq. (3.1), it is again seen that the instantaneous carrier frequency is linearly varying in time as $\omega' = t'/\beta_2 z$ under the SDW envelope. The pulse described by Eq. (3.1) is split into two copies where a delay, τ, is introduced onto one. Recombining the two pulses interferometrically yields a photocurrent at a subsequent photodetector proportional to,

$$\left|U_r(z,t)\right|^2 = \left| e^{j\frac{(t'-\tau)^2}{2\beta_2 z}} U(0,\omega'')\Big|_{\omega''=\frac{t'-\tau}{\beta_2 z}} + e^{j\frac{t'^2}{2\beta_2 z}} U(0,\omega')\Big|_{\omega'=\frac{t'}{\beta_2 z}} \right|^2. \tag{3.2}$$

For small delays relative to SDW duration (a condition easily satisfied in practice), the pulses overlap nearly completely, and the SDW envelope shape becomes of secondary importance. The square-law photodiode produces a cross-term with a linear phase proportional to the delay, τ. Equivalently stated, the two pulses interfere to form

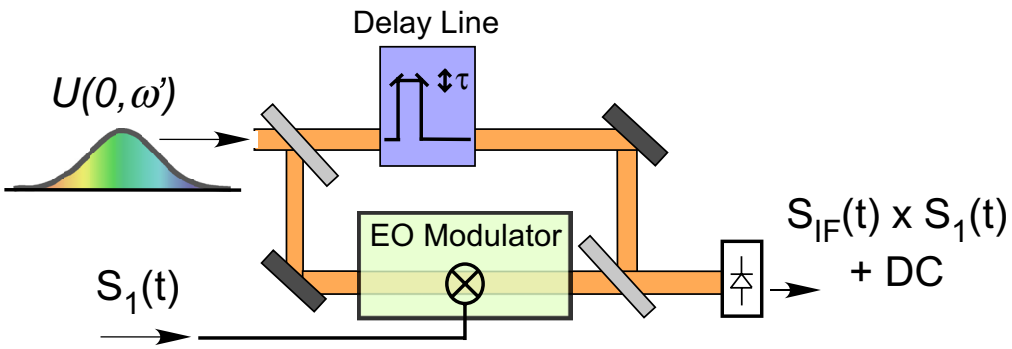

Fig. 3.1: Basic processing unit for microwave photonics with longitudinal SDWs. Coherent mixing in the Mach-Zehnder structure allows for microwave signal IF generation and manipulation.

$\omega_{IF} = |\omega'' - \omega'|$. From the interference, we can define a microwave IF signal, $s_{IF}(t)$, originating from the cross term,

$$s_{IF}(t) \propto \left| U(0,\omega') \Big|_{\frac{t'}{2\pi\beta_2 z}} \right|^2 \cos\left[\left(\frac{\tau}{\beta_2 z} \right) t - \frac{\tau^2}{2\beta_2 z} \right]. \tag{3.3}$$

Thus longitudinal SDWs lend themselves to the simple creation of delay tuned IF signals, where $\omega_{IF} = \tau / \beta_2 z$. The additional constant phase related to τ^2 in the cosine term is negligibly small and will be ignored. In practice, the usable range of generated frequencies can be as slow as the SDW envelope allows and as fast as the photodiode (and digitizer if required) allow for. In this dissertation, the range of IFs will cover ~100 MHz to 10's of GHz.

To perform microwave spectrum analysis and signal generation, an asymmetric Mach-Zehnder structure is offered as the basic processing unit. Fig. 3.1 shows a schematic of the processor. One arm of the interferometer is responsible for imposing the

controllable delay while the other introduces a microwave signal of interest, $s_1(t)$, using a high speed modulator. By imposing $s_1(t)$ onto one of the SDWs in Eq. (3.2), the two pulses recombine to form a cross term proportional to $s_1(t) \times s_{IF}(t)$. Spectrum analysis and signal generation differ based on whether the product is considered to be a projection, as in analysis, or to be envelope/carrier creation, as in signal generation.

3.2 Microwave Spectrum Analysis

Detection and analysis of microwave signals in the gigahertz to terahertz range is of critical importance to a variety of fields including RADAR/LIDAR, imaging, and astronomical detection [60,61]. Due to the limited speed and dynamic range of microwave digitizers [62], commonly employed electronic techniques rely on channelization of the signal bandwidth to provide high resolution spectrum analysis. Microwave photonics methods for spectrum analysis offer the potential to achieve wide instantaneous bandwidth in compact designs [15,58]. Recognizing the utility of the pulse shaping method in Section 2 for microwave spectrum analysis when the modulating signal is unknown, we modify that technique to demonstrate an approach for microwave spectrum analysis that exploits the bandwidth of longitudinal SDWs to process microwave signals without the technical challenge of recompressing the ultrafast optical signal. Specifically, using the basic processor of Fig. 3.1, a straightforward method for microwave spectrum analysis is realized with ultimate potential for analyzing signals with bandwidths approaching 100 GHz and with resolution less than 10 MHz [16].

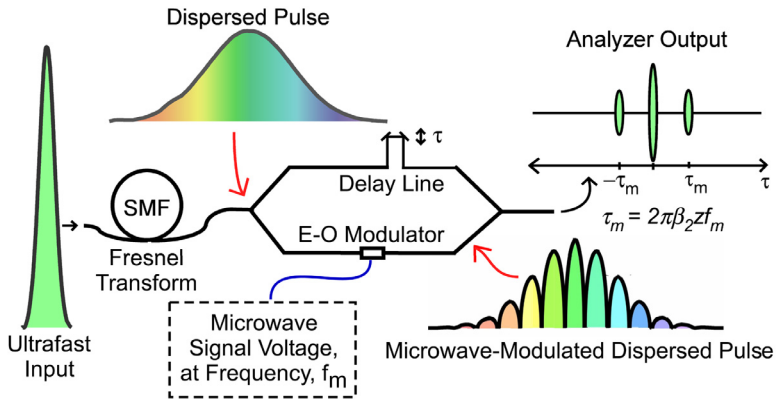

Fig. 3.2: Schematic diagram of the microwave spectrum analyzer shown. The signal voltage is a single RF tone with a bias. The correlation output shows the two sidebands and the central DC spike.

A schematic diagram of our approach is shown in Fig. 3.2. The front end is similar to that of the fiber-based pulse shaper. In the Mach-Zehnder processor an IF is generated as described by Eq. (3.3). For microwave signal processing, the IF serves as a delayed-tuned local oscillator (LO) sweeping over the modulation spectrum. Using a time averaged detector as a low pass filter (LPF), the system isolates that microwave signal component in $s_1(t)$ that is homodyned by the variable LO. A trace over all delays, equivalent to a cross correlation of the two pulses, shows correlation peaks for all spectral components of the microwave signal. This arrangement is analogous to an RF super-homodyne receiver.

An analytic description of the microwave spectrum analyzer proceeds in the time domain as in Eq. (3.3). Time-averaging the cross-term by the detector for time, T, leads to a signal,

$$\frac{1}{T}\int_0^T \left| U(0,\omega')\big|_{\omega'=\frac{t}{\beta_2 z}} \right|^2 s_1(t)\cos\left[\left(\frac{\tau}{\beta_2 z}\right)t - \frac{\tau^2}{2\beta_2 z}\right]dt \,. \qquad (3.4)$$

Thus as the time integration is lengthened the detection will isolate the component of *s(t)* oscillating at a microwave frequency, $\tau/(2\pi\beta_2 z)$. By varying the delays, all the spectral components of $s_1(t)$ can be determined from the correlation process.

Fig. 3.3 shows experimental results from a proof of concept experiment. We implement the system by first generating 150 fs pulses at 1.55 μm with the Coherent MIRA/OPO laser system. The pulses are dispersed in a free-space grating stretcher to the picosecond scale to lower peak power before they are launched into 25.2 km of SMF fiber. An optical spectrum analyzer is used to monitor and confirm no change in the spectrum of the pulse at the output of the fiber to assure that the propagation is linear. The generated longitudinal SDW is over 6 nanoseconds in duration. The polarization of the SDW is set with a polarization controller and a fiber coupled linear polarizer. This

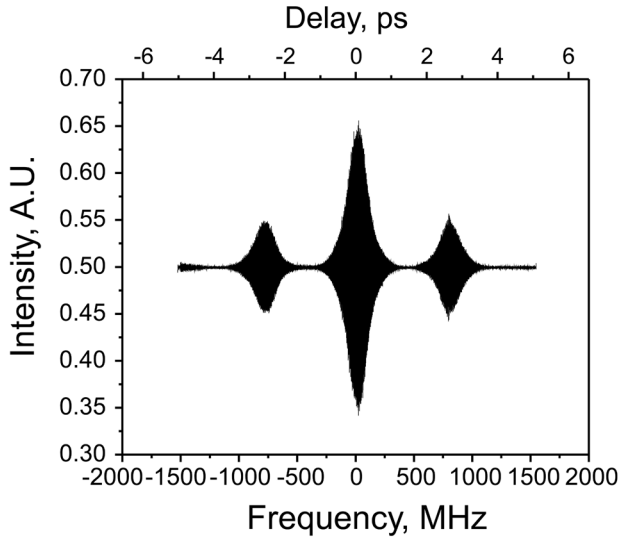

Fig. 3.3: Correlation trace from experimental proof of concept. RF signal consists of DC and 760 MHz components. Results are filtered in post-processing to remove background fluctuations. Upper axis gives temporal correlation delays as recorded. The lower axis shows a scaling of the delay axis to frequency: $f = \tau/(2\pi\beta_2 z)$.

waveform enters a free-space Mach-Zehnder arrangement where it is split; one copy is controllably delayed while the other copy enters a 1 GHz $LiNbO_3$ modulator. The modulator is driven by an RF source, which produces a 760 MHz tone locked in phase to the 76 MHz repetition rate of the laser (see following discussion). A bias accompanies the RF tone. Detection of the cross correlation is recorded in an InGaAs photodiode. The upper axis of Fig. 3.3 provides the correlation delays as recorded, while the lower axis makes use of the conversion of delay to frequency, $f = \tau/(2\pi\beta_2 z)$. The corresponding spectrum of $s_1(t)$, as read from the lower axis, confirms the DC term and oscillatory terms at ±760MHz. Viewing the upper axis the trace has peaks at the central point and ±2.4 ps ($2\pi\beta_2 z f_m = 2.4$ps if β_2=20ps^2/km, z=25.2 km, and f_m=7.6x10^{-4} THz).

The requirement of time-averaging introduces an experimental trade-off. In order that the LPF operation remains narrowband, long time integration is necessary. This additional time not only introduces latency, but also implies that more pulses from the pulse train will fall on the detector in a given integration window. The spectrum of the ultrashort pulse subsequently becomes discretized where the comb function multiplying the optical spectrum has a finesse related to the integration time. With respect to the operation of the microwave spectrum analyzer, the LO is discretized because the beat between a pulse pair can only constructively add to that of the next pair in the train at frequencies corresponding to multiples of the laser repetition rate. Ultimately, spectrum analysis produces a sampled version (Fourier series) of the microwave spectrum of *s(t)*. To produce a measurable signal when multiple pulses are averaged, our demonstrator analyzes an RF tone derived from a 10x multiplication of the repetition rate of the laser.

However, low repetition rate mode-locked laser pulses with large subsequent dispersion can generate SDWs that fill the entire integration window. If integration is matched to the pulse repetition period, the probability of intercept goes to unity while LO spectral discretization and the signal phasing requirements vanish.

Maintaining system frequency resolution over the full bandwidth of interest is important to spectrum analysis operation. The resolution of this method is locked to the time aperture created by the SDW and hence, the length of propagation in the dispersive element. To achieve 10 MHz resolution 100 ns SDWs are needed. While the LO can be tuned to frequencies approaching the bandwidth of the ultrashort pulse, at such delays the pulse pair is incapable of providing full LO resolution. The lack of pulse overlap reduces the effective time aperture and, by the uncertainty principle, degrades resolution. Current technologies limit EO modulation to the 100 GB/s and slower range. For such microwave signals, the amount of delay required to generate the LO is less than 10 percent of the pulse width, thus ensuring large pulse overlap. More significant than pulse overlap, higher order dispersion can reduce the TBWP by orders of magnitude as the LO resolution degrades quickly even at low frequencies. The topic of higher order dispersion impact on longitudinal SDW microwave photonics will be revisited in Section 3.4 as it applies commonly to both signal analysis and generation. As a final note, this microwave spectrum analysis approach is intended to provide wideband information instantaneously. To avoid the need for scanning and fully take advantage of the large instantaneous bandwidth that the short pulses offer, the space domain must be exploited. In such a manner variable delays are introduced in parallel and arrayed detection is employed to achieve correlation in space [63].

3.3 High Speed Microwave Signal Generation

Ultra wideband (UWB) microwave signals with arbitrary waveform are receiving much attention for their potential use in both RADAR systems and high-speed data links [64]. Their large fractional bandwidth provides multipath immunity, low probability of intercept, and high precision ranging capabilities. Low frequency spectral components also offer significant ground and material penetration. Conventional means for generation of UWB signals are limited due to the relatively slow speed of electronics for digital to analog conversion. Currently available arbitrary waveform generation devices operate up to only a few GHz. The desire to create UWB signals with carrier frequencies in the 10's of GHz and fractional bandwidths approaching 100% suggests investigating microwave-photonic approaches. A number of hybrid optical/electronic techniques for microwave and millimeter wave arbitrary waveform generation have been explored. Pulse waveform compression using dispersion was used to spectrally shift a 10 GHz tone to 15 GHz [65] but was limited in achievable frequency shift due to RF signal distortion. A similar approach with adaptive processing and an optical supercontinuum source produced RF signals in 1-12 GHz range [17]. These methods were further modified for operation with Talbot effect to produce highly compressed periodic waveforms [19]. However, all three of these methods are limited to generation of microwave sinusoids where signal modulation is restricted to frequency variation. Space-to-time optical methods offer an alternative approach to microwave arbitrary waveform generation [18,66,67], but these methods are limited to the TBWP of spatial pulse shapers. In these techniques, delayed and weighted optical pulses serve as samples for a desired electrical

waveform, which is generated through subsequent low pass filtering via detection of the pulse train envelope in a photodiode. A promising approach producing microwave tones through isolation and mixing of comb lines of a mode-locked optical source has demonstrated generation of 12.4 GHz microwave carrier with nanosecond scale envelope features [68]. This approach suggests a system to modulate the individual comb lines and mix via photodetection for complete microwave arbitrary waveform generation. However, the underlying shortcoming is that all the microwave tones are locked to the repetition rate of the original mode locked source. Thus the achievement of an arbitrary carrier frequency is greatly limited unless a serrodyne technique is employed. The system also loses power contained in all unused comb lines.

The high speed IF generated through the interference of two delayed, longitudinal SDWs offers as a path toward linear synthesis of UWB microwave signals. A method for microwave arbitrary waveform generation with independent envelope and carrier control derives from the manipulation of longitudinal SDWs in the basic processor unit of Fig. 3.1 [16]. Whereas, the microwave spectrum analysis technique relied on a slow integrating detector, the arbitrary waveform generation technique requires a fast photodiode to convert the IF into an electronic carrier frequency. Thus, to first order, at the output of the processor, photodetection and filtering creates a bipolar electrical signal with carrier, $f_m = \tau/(2\pi\beta_2 z)$. The EO modulator in one arm of the Mach-Zehnder interferometer defines the microwave envelope through the signal, $s_1(t)$. The time aperture of the longitudinal SDW sets a lower limit on the slowest realizable feature size or carrier frequency. Concurrently, the large optical bandwidth (>1 THz) makes fast

carrier generation achievable; however this number is practically limited by available photodetector speed. Envelope features imprinted on the pulse copy with the EO modulator are limited by the speed of the signal generator and modulator. An extension to signal generation with large fractional bandwidth for UWB is achievable if the processor were expanded to include multiple channels. As an example linear synthesis is possible with the introduction of a second modulated and delayed path, as suggested in Fig. 3.4, creating at the output a superposition of three modulated microwave carriers.

Our experimental approach is identical to that of Section 3.2 except for the use of an inline EDFA after the fiber spool and detection using a sampling oscilloscope with 30 GHz optical detector head. Additionally, a high pass filter is used to isolate the signal of interest from the DC term associated with the SDW envelope. Because of the interleaved sampling performed by the oscilloscope over multiple pulses, the modulator is again

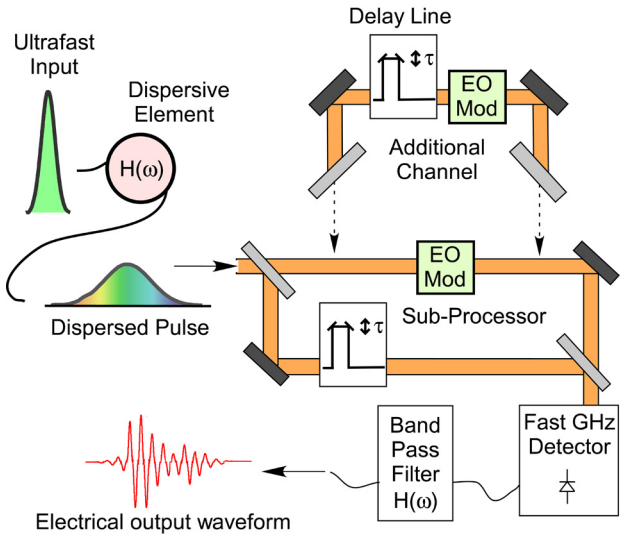

Fig 3.4: Schematic of our proposed method for electrical arbitrary waveform generation. Longitudinal SDWs are delayed and modulated before mixing in a fast square-law detector. A bandpass filter separates the DC terms to create a bi-polar signal. The superposition of channels leads to a linear synthesis of modulated microwave carriers at the output.

driven by sinusoids derived from harmonic of the laser repetition rate. This practice ensures that each modulated pulse contains identical envelope features. Fig. 3.5(a) shows an oscilloscope trace of a detected waveform for a delay τ=14.5 ps. The generated carrier is approximately 4.5 GHz. The subcarrier at 760 MHz is clearly visible. Large modulation depth is achieved by controlling the bias to the modulator. Fig. 3.5(b) shows a fast Fourier transform (FFT) of the detected signal samples plotted on a frequency scale. Results confirm the temporal waveform features.

The technique demonstrates high-speed microwave signal generation. The system offers independent control of the carrier and envelope. The TBWP of such a system is limited by the achievable time aperture (10-100ns) and maximum photodetector speed (~100 GHz) to values in the range of 10^3-10^4. Practical limitations to TBWP stemming from higher order dispersion are even more restrictive. These will be discussed next in Sect. 3.4. Additional channels would greatly improve the fractional bandwidth of generated signals, ultimately providing a path toward microwave arbitrary waveform generation.

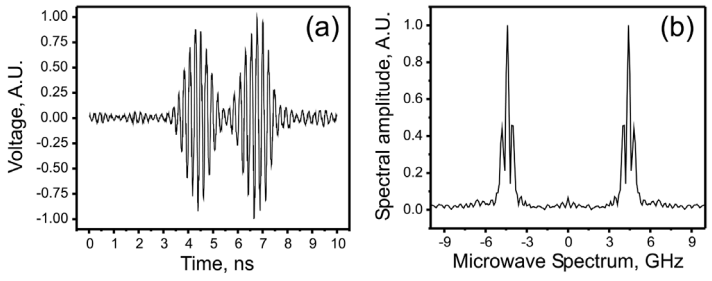

Fig. 3.5: (a) Oscilloscope recorded waveform from single channel realization of electrical arbitrary waveform generation technique. 3 GHz high pass filter removes the slow DC signal producing a bipolar waveform. (b) FFT of recorded waveform shows the 4.5 GHz carrier and 760 MHz envelope feature.

3.4 Impact of Higher Order Dispersion

Higher order dispersion can severely limit the realizable TBWP in longitudinal SDW applications. Fig. 3.6 graphically shows how higher order dispersion affects IF generation using the time frequency plots introduced in Fig. 1.5. The curvature of the longitudinal SDWs on the plots leads to a time variance in the instantaneous difference frequency. The beat signals following photo-conversion, shown below, develop a chirped IF with linewidth exceeding the transform limit, see Chapter 4 for a quantitative description. Furthermore, as shown on the right of Fig. 3.6, increasing delay to generate higher IFs, means that the linewidth increases as well. This process leads to a severe loss of resolution or signal precision depending on the application. A purely linear dispersive element could offer a path toward TBWPs exceeding 10,000 resolvable spots. To verify the improved performance of CFBG dispersion for IF generation, the study of Fig. 3.7 is included. Longitudinal SDWs from the 3M CFBG and 25 km of SMF were introduced

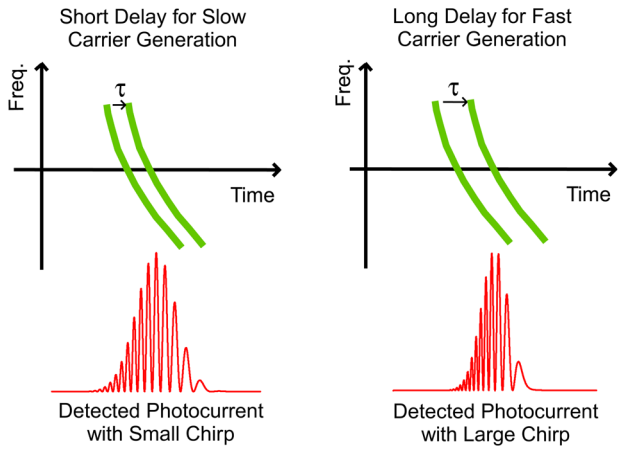

Fig. 3.6: Time frequency plot visualizations of longitudinal SDWs with β_3 distortion. The interference of two delayed copies (in green) produces the beat tone under the SDW envelope (red). For larger delays the detected photocurrent has a large microwave chirp. This chirp broadens the linewidth of the microwave signals used in the techniques of Sections 3.2 and 3.3.

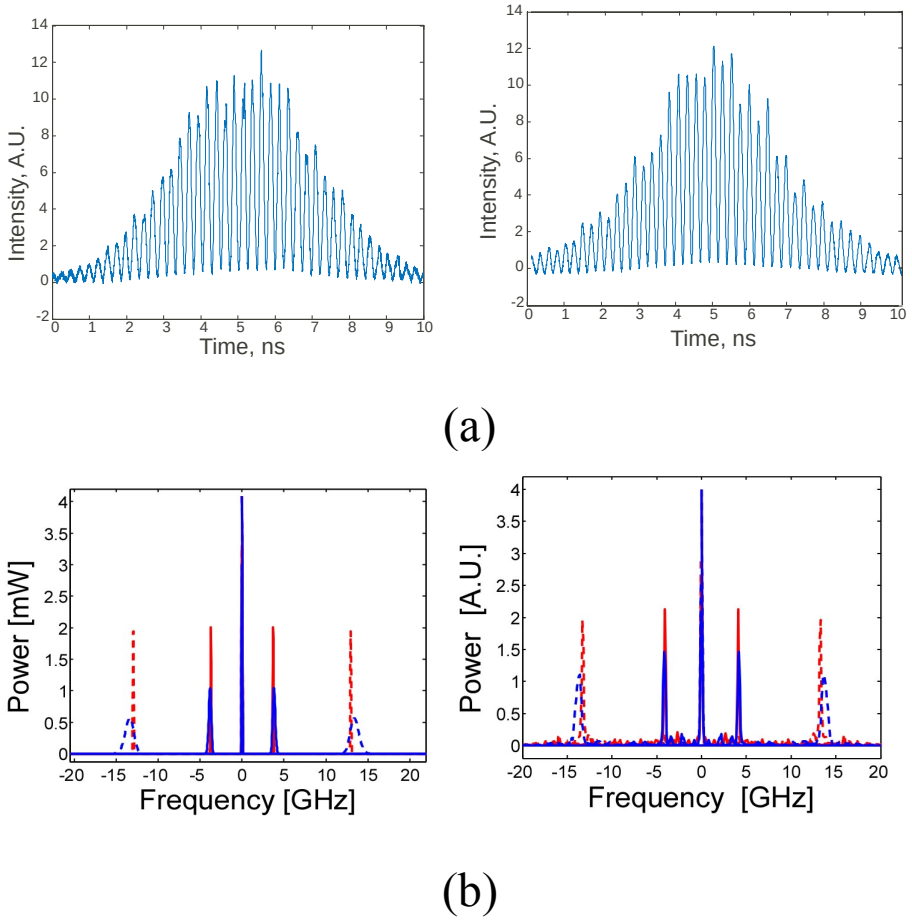

Fig. 3.7: A study of the effects of higher order dispersion on IF generation. (a) Time domain waveforms recorded after the basic processor of Fig. 3.1 with no $S_1(t)$ applied. The left waveform is from longitudinal SDWs generated in the linear CFBG while the right waveform is from SMF dispersed pulses. (b) The Fourier domain showing beat frequencies. The left is a simulated result while the right is experimental data taken from FFTs of waveforms as in (a). Red traces are from the CFBG while blue traces correspond to SMF. Clearly higher IF (longer delay between SDWs) leads to noticeable broadening of the SMF formed beat wave linewidth.

into the basic Mach-Zehnder structure. A static delay was used and no $s_1(t)$ signal was introduced, in order to create a narrowband IF. Fig. 3.7(a) shows example temporal signals recorded by a sampling oscilloscope with a 30 GHz photodetector plug-in. The CFBG and SMF derived SDWs are used on the left and right, respectively. Fig. 3.7(b) shows the interference signals in the frequency domain to illustrate linewidth

discrepancies. On the left a theoretical result from a system model is plotted while on the right experimental FFTs of captured data are shown. Note that for higher IF generation both the model and the experimental data show a degraded linewidth from the SMF as compared to the CFBG SDW. To quantify resolution loss, the fractional bandwidth of the IF is such that when the center frequency reaches 15 GHz, the linewidth exceeds 1 GHz. Unfortunately, at present birefringence in the CFBG, as discussed in Chapter 1, limits the ability to verify the CFBG processing benefit in a real system demonstration.

3.5 Summary and Acknowledgement

In summary, this chapter introduces two microwave photonic applications of longitudinal SDW signal processing. The unique time-frequency features of dispersed ultrashort pulses are exploited to generate narrowband microwave radiation capable of serving as either a local oscillator in a super-homodyne arrangement or as a carrier signal in a UWB signal generator. Both processors build from a basic free space, asymmetric Mach-Zehnder structure. Theoretical descriptions accompanying the demonstrations, provides a framework for understanding processing capabilities. Higher order dispersion is observed to limit achieved TBWPs. The arrival of an isotropic or polarization maintaining CFBG would greatly improve performance offered.

The text of Chapter Three, in part, is a reprint of the material as it appears in:
R. E. Saperstein and Y. Fainman, “Information processing with longitudinal spectral decomposition of ultrafast pulses,” Appl. Opt. **47**, A21-A31 (2008)
The dissertation author was the primary researcher and author. The co-authors listed in this publication directed and supervised the research that forms the basis for this chapter.

Chapter 4

Temporal Optical Frequency Domain Reflectometry using Longitudinal Spectral Decomposition

4.1 Introduction

The need for high-speed, high-depth-resolution imaging motivates interest in swept-frequency optical ranging [24-26,69-73]. The method borrows heavily from mature radar principles, which emphasize the importance of distributing signal energy over extended time apertures and reducing time domain sampling rates through intermediate frequency generation [74,75]. The range to target is deduced by simple measurement of the IF generated by interfering, identically-chirped target and reference signals after the target signal is delayed by a round trip to the target. All range information is contained in the time aperture of the frequency sweep. Thus this time domain realization of spectral interferometry or optical frequency-domain reflectometry (here referred to as time domain OFDR) has the potential for fast data acquisition rates in a scan-free approach [71-73]. When using longitudinal spectral decomposition to create frequency swept signals, IF formation proceeds as in the microwave-photonic

applications of Chapter 3 with the distinction that the delay between pulses in unknown. Within the last year, pulsed supercontinuum sources chirped in chromatically dispersive media have been used to demonstrate fine depth resolution with sub-microsecond sweep durations [24,25]. In these works record speeds for optical coherence tomography (OCT) A-scans were achieved using high-speed temporal sampling. These record speeds are attributable to the optical bandwidths supported by and sweep speeds created by fiber-based, passive dispersion technologies. Wideband pulsed sources chirped in such dispersive media promise to enable time domain OFDR systems with micron scale resolution over centimeter ranges.

As treated through the applications in Chapters 2 and 3 (or for instance in [76]), all longitudinal SDW processing systems exhibit aberrations in the presence of significant higher order dispersion, which causes a departure from the first order mapping of optical frequency to time delay. Linear CFBGs, designed specifically to disperse a pulse with all higher order terms set to zero such that a constant chirp rate emerges, are an important technological solution. Owing to the lack of polarization sensitive processing required in the reflectometry approach, CFBG birefringence can be ignored, and the analysis and demonstration of several key processing advantages afforded by linear CFBG usage in moderate- to low- resolution time domain OFDR can proceed. While the approaches leveraged in this chapter derive from RADAR practices, the passive dispersion characteristics of the linear CFBG allow for uniquely optical implementations.

The chapter is organized as follows: Section 2 introduces a time domain OFDR system utilizing the linear CFBG and compares the realization to earlier work and to a

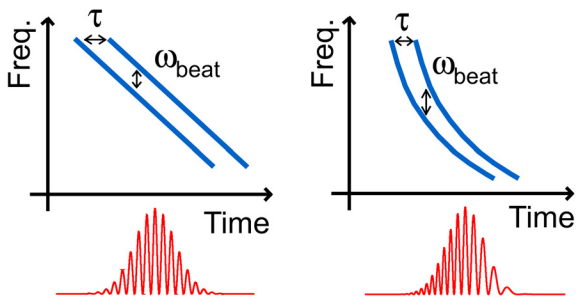

Fig. 4.1: Time-frequency visualizations of chirped pulse pairs. The plot on the left represents the favorable case of precise linear chirp generated by an ideal dispersion source such as the linear CFBG. The plot on the right illustrates the degrading effects of higher order dispersion. The lower portion of the figure gives a representative interference signal for each case.

traditional OFDR implementation, Section 3 demonstrates an effective and straightforward method for Doppler-range decoupling through the use of a two pulse sequence from the linear CFBG. Section 4 introduces dispersion-last time domain OFDR and demonstrates Doppler-immune ranging, and Section 5 summarizes.

4.2 Linear CFBG OFDR System

Time domain OFDR deduces target range from the beat frequency between two identically chirped target and reference pulses, one delayed relative to the other. A thorough mathematical treatment of the dispersion-based technique can be found in Ref. 25; a time-frequency visualization plot is presented in Fig. 4.1. Briefly, the spectral phase of a chromatically dispersed pulse is Taylor expanded around a carrier as in Eq. (1.8),

$$-\Phi = -\Phi_0 - \Phi_1\omega - 1/2\,\Phi_2\omega^2 - 1/6\,\Phi_3\omega^3 - \ldots \tag{4.1}$$

where again $\omega=\Omega-\omega_c$ if Ω is absolute frequency. Terms of orders higher than the dominant aberration, Φ_3, are ignored here but can be taken into account if needed.

Arrival times of the frequency components of the pulse are given by the negative derivative of the spectral phase:

$$t = -\frac{\partial \Phi}{\partial \omega} = \Phi_1 + \Phi_2 \omega + \frac{1}{2}\Phi_3 \omega^2 . \tag{4.2}$$

If time is referenced to the arrival of the carrier, we can work with relative time, $t' = t - \Phi_1$. Eq. (4.2) can also be inverted to find the instantaneous frequency arriving at a given time, t'. After reflection off a linear CFBG, where Φ_3 and higher terms equal zero, the arriving instantaneous frequency is chirped linearly with time under the pulse envelope according to

$$\Omega_{inst}(t') = \omega_c + t'/\Phi_2 \tag{4.3}$$

A delay, τ, between pulse copies generates a difference (beat) frequency in the interference term after square-law detection,

$$\omega_{beat} = \Omega_{inst}(t') - \Omega_{inst}(t' - \tau) = \frac{\tau}{\Phi_2}, \tag{4.4}$$

at all points in time under the envelope, see the left side of Fig. 4.1. Eq. (4.4) is derived from purely frequency domain arguments but leads to an identical IF result as the time domain approach in Eq. (3.3). Given the known dispersion parameter, Φ_2, the captured beat frequency may be converted to delay, τ, and hence target range, with resolution limited by the bandwidth of the system. In contrast, when a dispersion element with a third order response is employed, the arriving instantaneous optical frequency in the dispersed pulse is chirped nonlinearly as

$$\Omega(t') = \omega_c + \sqrt{\frac{2t'}{\Phi_3} + \left(\frac{\Phi_2}{\Phi_3}\right)^2} - \frac{\Phi_2}{\Phi_3}. \tag{4.5}$$

This situation is visualized in the right side of Fig. 4.1, where it is clear that a time-variant beat frequency,

$$\omega_{beat} \approx \frac{\tau}{\sqrt{2\Phi_3 t' + (\Phi_2)^2}}, \tag{4.6}$$

forms between detected pulse copies under delay. (The approximation in Eq. (4.6) assumes $t' \gg \tau$, valid through most of the detection time when the delay, τ, is much shorter than the pulse duration.) When converting the beat frequency of Eq. (4.6) to target range, the apparent line broadening drastically reduces measurement resolution at modest to large ranges or delays.

The optical chirp characteristics of passively dispersed short pulses have major ramifications for the implementation of time domain OFDR systems. Both prior demonstrations of dispersion-based time domain OFDR employ dispersive sources with significant higher order dispersion [24,25]. The measured beat signals in these experiments are time-variant, as in Eq. (4.6), and digital post-processing is required to compensate for higher order phase distortions. From a physical perspective the ranging technique is a time domain realization of OFDR. Therefore, to maximize resolution, a defined time/frequency map must instruct a data interpolation algorithm to sample the signal at times corresponding to the temporal arrival of regularly-spaced optical frequency components. As an example, one could resample a signal with spectral arrival times given by Eq. (4.5) at times t'' such that

$$t' = t'' + \frac{\Phi_3}{2}\left(\frac{t''}{\Phi_2}\right)^2 \tag{4.7}$$

in order to create regularly spaced frequency samples. The process effectively converts the right side of Fig. 4.1 to the idealized picture on the left side. If the interpolated samples are placed on a regular grid, a simple fast Fourier transform (FFT) provides accurate, bandwidth-limited depth resolution at all ranges. Inherent to the approach is the assumption that the beat frequency is very small compared to the bandwidth.

Time domain OFDR employing higher order chirped sources requires both the creation of an accurate time/frequency map and the continual triggering of the interpolation algorithm at an appropriate start time corresponding to the arrival of the carrier, ω_c, around which the Taylor expansion of Eq. (4.1) is constructed. Failure to satisfy either requirement leads to loss of both relative and absolute range accuracy. In practice the time/frequency map can be extracted using a standard dispersion measurement as in Ref. 24 or through an analysis of the interference phase of a target and reference pulse under known delay as in Ref. 25. The latter method is particularly appealing for its ability to include phase distortions from many potential sources. However, like its spectral domain counterpart [77], using a time domain spectral-shearing interferometer for pulse phase extraction requires that the delay between pulse copies used for calibration be known with high accuracy. Simple analysis shows that a relative error, R, in pulse-to-pulse delay during calibration introduces a scaling factor (1+R) into all subsequent delay measurements to which the calibration is applied. As this ranging technique aspires to achieve and exceed 10^4 resolvable spots, the 1+R factor can lead to appreciable depth-dependent inaccuracies. Thus the reference arm requires a translation

stage with a large number of resolvable spots and knowledge of the zero delay offset point. In the case of a linear chirp, on the other hand, where only relative delays between targets in the image are relevant, such precision is unnecessary. With respect to triggering, system accuracy critically depends on applying the time/frequency map at the correct time (Φ_1) relative to pulse arrival. In real time operation, an external trigger derived from the pulsed laser source should be synchronized with the interpolation algorithm. This approach allows the map to be anchored at Φ_1 in all pulses within the picosecond trigger jitter of commercial digitizers. Signal inspection to identify Φ_1, as in Ref. 24, using the real time Fourier transformation principle [11,78], is limited by the temporal resolution of the detector. However, for the distortion-canceling, irregular sampling methods using an external trigger, whenever the trigger is lost, the time/frequency map needs recreating before re-application.

To simplify system implementation, while addressing the potential range inaccuracies stemming from both time/frequency map generation and misidentification of Φ_1, we demonstrate a time domain OFDR system driven by sub-picosecond pulses dispersed in a linear CFBG. All calculations follow from the simplified analysis of Eqs. (3) and (4). As the beat signal frequency is time-invariant, locating Φ_1 is not experimentally critical. The beat signal linewidth also does not broaden at extended ranges, thus irregular sampling is not required to provide accurate ranging results over a large number of resolvable spots. Our demonstration in this work is practically limited to moderate/low resolution OFDR. For a system employing optical bandwidths sufficient for high resolution OFDR, phase distortions both common and unshared between reference and target pulses quickly degrade resolution despite the use of linear CFBGs.

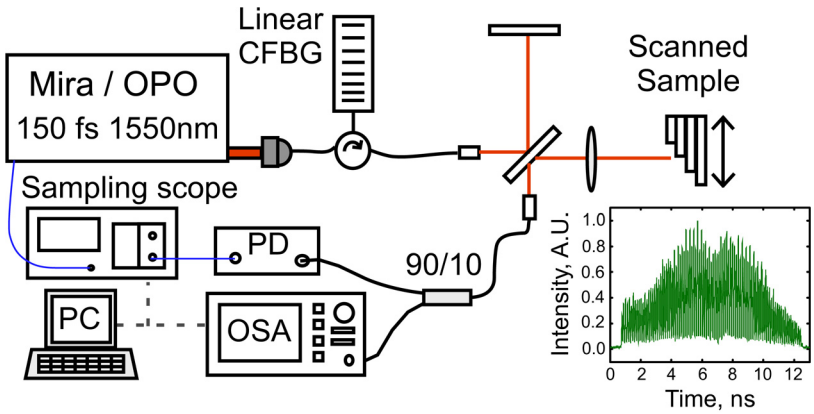

Fig. 4.2: Schematic of experimental setup. PD is the amplified photodiode, OSA is the optical spectrum analyzer, and PC is a personal computer. The inset shows sampling scope data captured for a single point reflection.

Potential distortion sources include the use of non-transform limited launch pulses, group delay phase ripple within the CFBG, and dispersion of the target sample. The ability to compensate these effects in the physical domain is strained. For high resolution OFDR interpolative post processing is likely required in such a system. A number of works have shown the capabilities of post-processing to compensate for dispersive effects in OFDR [79,80]. These techniques are all relevant for application to time domain OFDR based on dispersed pulses. However, noting the loss of resolution at extended depth ranges in Ref. 24 despite interpolative data re-sampling, it is clear that high resolution time domain OFDR benefits from the minimization of total accumulated higher order phase in the physical layer before photo-detection. For short pulse signals, such dispersion is offered by linear CFBGs.

Our experimental demonstrator is depicted in Fig. 4.2. The source is a Ti:Sapphire pumped OPO creating 150 fs pulses at wavelengths in the conventional telecommunications band around 1550nm. No nonlinear spectral broadening is employed. The pulses are fiber launched with powers below the threshold for optical

nonlinearities and are dispersed in a 3M Corp. CFBG offering Φ_2=-431.6ps^2 (2711 ps/THz) of dispersion over a 35nm bandwidth centered at 1550nm. A loss of 4dB is incurred in the grating and required circulator. As noted in Table 1.1, the dispersion to loss ratio is quite similar to that of SMF. The tailored CFBG provides pure chromatic dispersion with all higher order dispersion terms approximately zero. Additional fiber patch cables adjust the measured dispersion value to Φ_2=-432.4ps^2. Due to system bandwidth, the higher order dispersion in these meters of cabling is assumed negligible. After dispersing, the pulse time aperture approaches 12 ns: a conservative match to the pulse repetition period and data collection window of 13 ns. As the beat signal synchronously repeats at the pulse repetition frequency but is not restricted to harmonics of the repetition rate, data taken over a time aperture covering multiple pulses in the train can produce destructive interference for the signal beat and should be avoided. The dispersed pulses are introduced into an interferometer for processing. A Michelson arrangement is used to demonstrate system performance. The target arm contains focusing optics and a translating reflective sample. The staircase-like sample target assembled either from 1mm thick gold coated microscope slides or from 150 μm thick gold coated cover glass is stepped through an 80-point one dimensional scan. The reference arm is biased to ensure all delays are positive. Ninety percent of signal power is directed to a 15GHz amplified photodiode (Agilent 11982A). The 15 GHz 3dB roll-off point corresponds to a range of 6.1 mm. The signals digitize in an Agilent sampling oscilloscope with an effective interleaved sample spacing of 3.2ps. This detection method exceeds by nearly an order of magnitude the current state of the art in real-time sampling rates but is used here to enable the demonstration of other system capabilities.

The remaining ten percent of signal power goes to a commercial fiber coupled optical spectrum analyzer (OSA) (Ando 6317B) with .01 nm resolution. Assuming Nyquist sampling, the resolution leads to a range limit of 60 mm. A personal computer controls sample translation and data processing.

An examination of data captured from a single representative reflection point gives insight into system performance. A time domain waveform captured by the sampling scope is shown as inset in Fig. 4.2. An FFT of this waveform, Fig 4.3(a) red line, presents the information in the beat-frequency domain. The frequency axis is scaled to target range using the factor $\Phi_2 c\pi$ where c is the speed of light and Φ_2=-432.4 ps^2. Corresponding to the single reflection surface at a range of 3.22 mm, a single spike is present in Fig. 4.3. The raw data is plotted against a linear amplitude scale and is normalized to the peak of the point spread function (PSF). Resolution is measured at 52 microns, full width at half maximum (FWHM), for the PSF. This resolution is consistent with the bandwidth of the source (<3.5 THz FWHM) and matches well with the 51 μm FWHM of the DC component. Note that the DC and harmonic components would have identical width were the beat signal an ideal sine wave. The axial resolution offered is sufficient for moderate-to-low resolution ultrafast metrology but falls short of the resolutions required for biomedical OCT applications. A broader-band source is expected to bring the resolution down to the 35 μm transform limit of the CFBG bandwidth with the penalty of increased side lobes. To cancel deterministic amplitude noise, the signal is divided by a time averaged copy of the reference pulse and re-

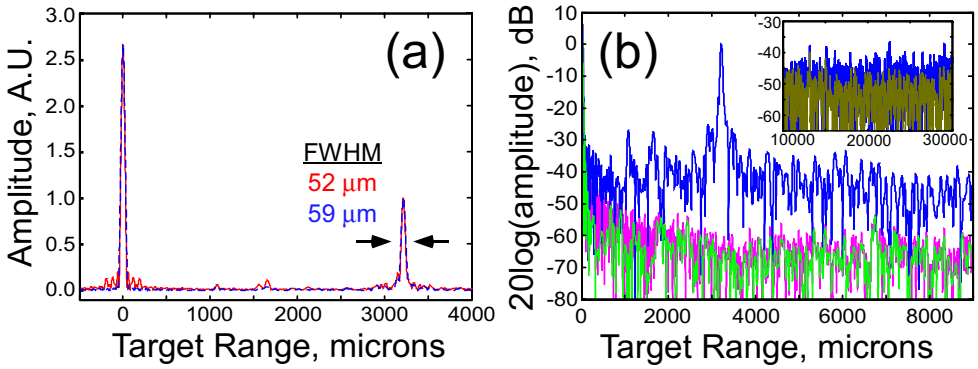

Fig. 4.3: Representative waveform from a single point reflection transferred to the range domain by an FFT operation. (a) Linear amplitude plot shows point spread function. Red line is the raw collected data, while the blue line is normalized by the background and reshaped using a Hamming window. (b) Log plot of power spectral density for point spread function. The blue line represents the reshaped data signal while the magenta and green lines show noise equivalent responses from the amplified photodiode using Hamming and Blackman reshaping windows, respectively. The inset shows that at larger ranges background can be reduced through a 4x averaging (dark yellow) as compared to non averaged (blue).

windowed with a Hamming function (blue curve in Fig. 4.3(a)). The procedure strongly reduces much of the short range noise under 1000 microns at the expense of broadening the linewidth to 58 microns. It is important to note that higher frequency (longer range) deterministic spurs, arising from amplitude ripples in the CFBG etc., can not be fully cancelled in this manner. These frequency components in the signal slip out of phase with their counterparts measured from the reference arm alone. This effect accounts for the inability of the reshaping approach to completely remove the two spurious reflections around 1100 and 1600 microns. The issue may subside in practice when target signals are much weaker than reference signals. In Fig. 4.3(b) the power spectral density of the reshaped signal of Fig. 4.3(a) is displayed on logarithmic scale, again in blue. The response is normalized to the peak reflection signal. The dynamic range (DR) of the system is limited by spurs to roughly 26 dB. This DR is significantly impacted by

spurious reflections in the source and optical system and from group delay ripple in the linear CFBG, whose physical manifestation can be treated like an accumulation of many weak reflected signals [81]. Each spurious reflection contributes small spikes, distributed in range, to the plots of Fig. 4.3. Apart from the spurs, much of the high frequency (ranges > 10000 microns) noise can be attributed to source jitter incurred over the extended time of interleaved detection. In a single pulse, real time implementation, jitter should only impact the ability of post processing to remove deterministic aberrations. However, for this multi-pulse demonstrator, 4x averaging can be seen to lower the background signal by 4 dB, shown inset to Fig. 3(b).

System sensitivity is gauged by the noise equivalent response. The magenta line of Fig. 4.3(b) shows the output with the sample arm blocked. The reference pulse alone is detected as before, including the amplitude reshaping process. The sensitivity value is -58 dB in Fig. 4.3(b) while typical values lie between -55 and -56 dB. These values are made by comparing the peak signal response to the level of the noise one standard deviation above the mean for range values of interest, as done in Ref. 25. Switching from a Hamming window to a narrower Blackman filter improves the sensitivity values by 2 dB at the expense of losing 2-3 μm of resolution in the signal peak (see the noise floor reduction in the green curve of Fig. 4.3(b)). Reference measurements employing SMF as the dispersion source showed sensitivities of comparable value to those included here. The comparison result suggests that sensitivity is dominated by source and detector characteristics. Time domain OFDR systems are typically limited in sensitivity by laser source relative intensity noise (RIN) requiring the use of dual balanced detection [72,73]. The RIN fluctuations manifests themselves as spurs in range measurements, like Fig.

4.3(b), thus elevating noise levels. However, to contribute negatively the periods of RIN fluctuations must be shorter than the observation window; otherwise they affect only "DC" values. For the slow, actively-swept sources used commonly in time domain OFDR, the degrading RIN is that of a typical continuous-wave laser source. With time domain OFDR based on dispersed ultrashort pulses, single pulse acquisition over a short observation window is the desired operating approach. The mapping of the modelocked spectrum to time implies that RIN will arise from mode-partition noise as was recently studied in Ref. 82. A formal introduction of RIN treatment based on this new theory is compounded by the multi-pulse, interleaved acquisition in use in our demonstrator. While it is permissible to state that observed dynamic range values are comparable to Refs. 24 and 25 where interpolation post-processing is utilized, the lack of formalism including all system parameters prevents comparison of sensitivity values.

Representative one dimensional surface scans are shown in Fig 4.4. In each of these 80-point scans, data taken using time domain OFDR is plotted in green while conventional OFDR data is plotted in black. The conventional OFDR data is acquired by scanning spectrometer and then interpolated using a wavelength to frequency mapping [83]. Both the time domain OFDR and conventional OFDR data were zero-padded by a factor of 32 for range-domain interpolation at the single micron scale. Fig. 4.4(a) shows two overlaid scans across the sample made of 150 micron cover glass plates in a staircase arrangement. In the upper trace the reference mirror was biased to demonstrate precision at larger ranges. Fig. 4.4(b) shows a single scan made over the larger sample of millimeter size microscope slides. Note that the time domain acquisition surpassed the 3dB roll-off point, 6.1 mm, of the high speed detector considerably with minimal penalty

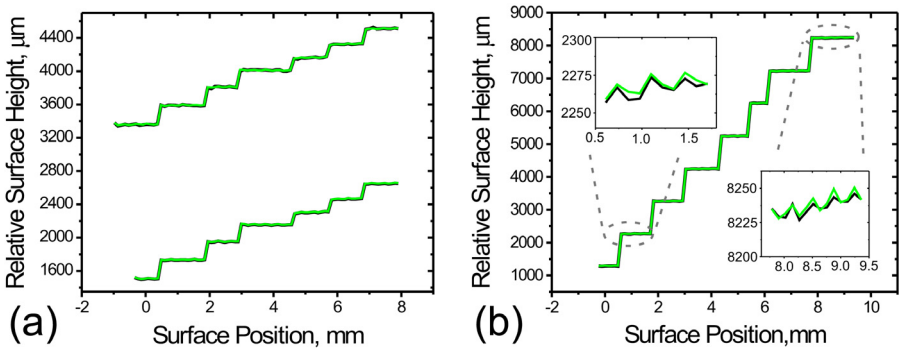

Fig. 4.4: Relative height measurements over gold-coated staircase surfaces. The green traces are the time domain realization of OFDR while the black traces are captured using conventional OFDR. (a) Two overlaid scans from the same surface composed of ~150 micron cover glass plates. The reference arm is moved to emphasize single point precision over various ranges. (b) A single scan covering seven 1 mm slide glass steps. The insets show that the measurement precision remains under 25 microns over the entire range.

observed within the measurement. Zoom-in insets show that noise variance does not increase over the range. The slight upward trend of measured height with surface position noticeable in each inset graph is attributed to surface slope and is not present in (a). In Fig. 4.4 very good agreement is seen between time domain and conventional OFDR despite the dramatic difference in data acquisition time windows of the two OFDR techniques.

Although Fig. 4.4 shows a noise floor on a single flat surface lower than the FWHM of the PSF in Fig. 4.3, the latter constitutes a fairer metric of system resolution. The single scan in Fig. 4.4(b) provides ~50 micron resolution over 7 millimeters, thus demonstrating 140 resolvable range spots for the time domain OFDR system. In accordance with the analysis of Ref. 25, the number of resolvable spots (e.g. system time-bandwidth product) of this time domain OFDR systems is fundamentally limited to the product of time aperture and detector bandwidth. Here, a 13ns time window and 15 GHz

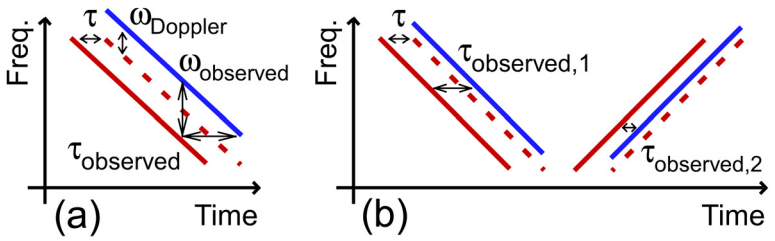

Fig. 4.5: Time-frequency visualizations of chirped reference and target pulses. The target pulse (dashed) is delayed with respect to the reference (red solid) and upshifted via Doppler (blue). (a) Doppler upshift lead to a larger observable beat frequency and apparent target range. (b) A two pulse sequence with opposite chirp signs generates two distinct observable ranges.

detector imply an upper limit of 195 resolvable spots. The discrepancy between our 140 points and the theoretical limit can be attributed to our underutilization of available reflection bandwidth (3.5 THz of 4.3 THz max) and system time window (12ns of 13ns max). Demonstrated results show that time domain OFDR realized with the linear CFBG can deliver accurate ranging values over extended total ranges on the sub-microsecond time scale. Moderate to low resolution systems can exploit the linear CFBG technology to possibly forego interpolative data post-processing.

4.3 Doppler-Range Decoupling

A practical problem facing conventional ranging systems employing frequency swept signals is the coupling of range and Doppler information in the return target signal. Fig. 4.5 gives a time/frequency visualization showing how an unexpected Doppler upshift, $\omega_{Doppler}$, to a target pulse will be recognized by the system as an additional apparent delay. The problem has been long known in Radar signal processing [84] and has the potential to cause ambiguous results in a time domain OFDR system [85]. A common approach to Doppler-range decoupling is to increase the number of degrees of freedom in the system

by utilizing a pulse sequence of non-identical chirps. The linear CFBG technology is well suited for a two pulse measurement in which the first pulse is dispersed with the blue side of the CFBG and the second pulse with the red side of the same grating. Fig. 4.5(b) gives a visualization of the two pulse sequence. The passive dispersion provided by the two-port linear CFBG allows for near perfect signal conjugation or chirp sign flip between the two pulses. It can be seen that this sign flip will allow for maximum contrast between Doppler and range information.

To understand the utility of the two pulse sequence it helps to theoretically derive the instantaneous frequency of a dispersed and Doppler shifted pulse. Due to the time-variance of the Doppler phenomenon, standard frequency-domain transfer function techniques cannot be employed (a Doppler element generates frequencies at the output that are not present at the input). However, the complex electric field of a chirped Gaussian pulse reflected from a linear CFBG can still be written as a superposition of time exponents:

$$E(t') = E_0 \int_{-\infty}^{\infty} e^{-\frac{1}{2}\frac{(\Omega-\omega_c)^2}{\Delta\omega^2}} e^{-j\frac{1}{2}\Phi_2(\Omega-\omega_c)^2} e^{j\Omega t'} d\Omega \,. \tag{4.8}$$

Again ω_c is the carrier frequency, and $\Delta\omega$ is the 1/e point spectral half-width. E_0 is included to scale the field amplitude. In keeping with the formalism for linear CFBG dispersion, the pulse travels in the moving reference frame, t', and the second order dispersion (quadratic phase) term is present while higher order terms are absent. When the Doppler shift acts on the chirped pulse, it stretches or compresses t' through a factor

$\alpha = \left(1 - 2\frac{\mathrm{v}}{\mathrm{c}}\right)$, where v is the velocity of the target projected onto the illumination direction and c is the speed of light [84]. The Doppler-shifted dispersed pulse is therefore given by:

$$E(t') = \alpha E_0 \int_{-\infty}^{\infty} e^{-\frac{1}{2}\frac{(\Omega-\omega_c)^2}{\Delta\omega^2}} e^{-j\frac{1}{2}\Phi_2(\Omega-\omega_c)^2} e^{j\Omega\alpha t'} d\Omega. \tag{4.9}$$

The term, α, also scales the amplitude to include the increase or decrease in photon energy accompanying reflection from the moving target. Completing the square and taking the integral over the Gaussian, the output signal in time is:

$$E(t') = \frac{\alpha E_0 \sqrt{2\pi}}{\sqrt{\Delta\omega^{-2} + j\Phi_2}} e^{-\frac{(\alpha t')^2}{\Delta\omega^{-2} + j\Phi_2}} e^{j\omega_c \alpha t} \approx C e^{-\frac{1}{2}\frac{(\alpha t')^2}{\Delta\omega^2 \Phi_2^2}} e^{j\left(\omega_c \alpha t' + \frac{1}{2}\frac{(\alpha t')^2}{(\Phi_2)}\right)}. \tag{4.10}$$

Simplifications in the exponents are valid when $1/\Delta\omega^2 \ll \Phi_2$, which is easily satisfied for the bandwidths and dispersion values used for time domain OFDR. Taking a derivative of the phase in Eq. (4.10), the instantaneous frequency under the pulse envelope is given by:

$$\Omega_{inst}(t') \approx \alpha\omega_c + \frac{\alpha^2 t'}{\Phi_2} = \alpha\left(\omega_c + \frac{\alpha t'}{\Phi_2}\right). \tag{4.11}$$

As expected, Doppler processing up- or downshifts the chirped signal carrier by the factor α relative to the dispersed-only pulse of Eq. (4.3). The appearance of α^2 in the linear temporal sweep term is due to the combined effect of the frequency dependence of Doppler shifts and the variation in return time from the moving target. Following the

measurement approach of time domain OFDR, the difference frequency (under the interaction envelope) between a dispersion-only frequency sweep of Eq. (4.3) and a delayed version of the Doppler shifted swept signal of Eq. (4.11) is

$$\omega_{beat}(t') \approx \alpha^2 \frac{\tau}{\Phi_2} + (1-\alpha)\omega_c \frac{2\mathrm{v}}{\mathrm{c}} + \frac{t'}{\Phi_2}\frac{4\mathrm{v}}{\mathrm{c}} \approx \alpha^2 \frac{\tau}{\Phi_2} + \omega_c \frac{2\mathrm{v}}{\mathrm{c}} + \frac{t'}{\Phi_2}\frac{4\mathrm{v}}{\mathrm{c}}. \quad (4.12)$$

Comparison with Eq. (4.4) reveals the impact of target motion on the beat signal. The α^2 stretch factor in the first term, within the sensitivity of a typical measurement, is indistinguishable from unity. The second term imparts the expected Doppler shift to the measured beat frequency. The last term leads to a time variant beat frequency and must be considered more closely. Its consequences are easier to observe when the beat frequency is converted to target range using the scale factor $\frac{1}{2}c\Phi_2$. We denote by R_1 and R_2 the two apparent range values obtained with the two probe pulses. Let the first pulse reflect from the blue side of the CFBG, $\Phi_2<0$, and the second from the red side, $\Phi_2>0$, then the range values are:

$$R_{1,2} = \frac{c}{2}\left(\tau \pm |\Phi_2|\omega_{\mathrm{Doppler}}\right) + 2t'\mathrm{v} \quad (4.13)$$

where $\omega_{\mathrm{Doppler}}=-\omega_c 2\mathrm{v}/\mathrm{c}$. The potential loss of resolution from the line broadening as a result of the $2t'\mathrm{v}$ term equals twice the product of the time aperture and the target velocity. If this product is much less than the range resolution, it can be ignored. Alternatively, resolution may be recovered with an interpolative post processing approach as discussed earlier. For a time domain OFDR system with supercontinuum bandwidths, as in Ref. 24, the time variance of the beat frequency due to significant

Doppler shifts cannot be ignored if micron-scale resolution is to be preserved. Whether or not the $2t'v$ term is included, the range and Doppler information are readily separated when both R_1 and R_2 are available. Averaging the two range values delivers a true Doppler-free range, while subtracting R_2 from R_1 and dividing by $2c\Phi_2\pi$ yields the Doppler shift (in frequency units). To avoid measurement ambiguity, the setup must be configured so that $\tau > |\Phi_2|\omega_{Doppler}$. A simple biasing of the reference delay allows this restriction to be easily met in practice. Two oppositely chirped pulses provide the best contrast between range values, R_1 and R_2, for a given dispersion strength and are easy to obtain by reflecting off the two sides of the linear CFBG. Thus the isolation of true Doppler shift and range values is made in a straightforward and accurate manner by incorporation of linear CFBG technology.

In the demonstrator introduced in Section 4.2, the coupling factor, $\Phi_2 c\pi$, corresponds to roughly 0.4 μm of range shift per MHz of Doppler shift, or equivalently, to ~0.5 μm of range shift per m/s of parallel target velocity. Coupling would be greater, however, in a system utilizing stronger dispersion, while tighter error tolerance would be imposed by bandwidth-driven resolution improvements. Time domain OFDR with 10^4 resolvable spots over centimeter-scale ranges requires, as compared to our experimental setup, a ten fold increase in system bandwidth, a further five fold increase in dispersion strength of the CFBG, and a corresponding decrease in pulse repetition rate. A system with these specifications should be concerned with high-speed blood flow coupling to range values in a biomedical application [86,87]. Additionally, as the utility of the OFDR technique extends beyond biological imaging to metrology for targets with larger

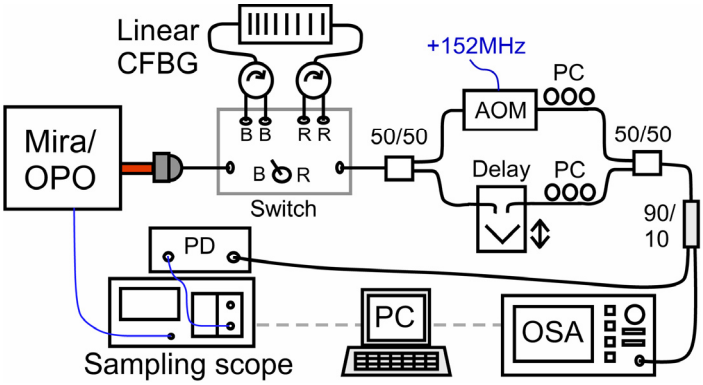

Fig. 4.6: Schematic of Doppler-range decoupling demonstrator. A switch controls the side of the CFBG off which the short pulse disperses. A fiber Mach-Zehnder interferometer introduces a controllable delay between chirped pulses while Doppler shifting one by + 152 MHz. Polarization controllers (PC) align the signals before coupling. 90% of the signal goes to a PD for time domain OFDR while the remainder goes to an OSA for conventional OFDR.

depth features and potentially faster flow/travel rates, separation of Doppler and range information becomes increasingly important.

To demonstrate the ability of the two pulse sequence to decouple Doppler and range values, the experiment described in the preceding section is modified according to the schematic shown in Fig. 4.6. The fiber coupled pulse enters a manual switch box that passes the pulse to the blue or red port of the CFBG. Reflections from either side are switched back to the remainder of the system. The 50 micron resolution limit puts an initial restriction on observable Doppler shifts. For our demonstrator we use a +152 MHz acousto-optic modulator (AOM) from IntraAction Corp. to provide a Doppler upshift to the signal pulse, equivalent to target velocity ~-120m/s. The frequency shift corresponds to an apparent range shift of ±60 microns depending on chirp sign. The fiber coupled AOM is incorporated into the target arm of a Mach-Zehnder interferometer. The reference arm contains a fiber coupled delay line to demonstrate the functionality of the system at multiple ranges. The time variant term in Eq. (4.13) is here neglected because

it yields only a 3 micron variation over the entire 13 ns observation time window. The AOM is driven by a filtered and amplified signal derived from the 2nd harmonic of the laser repetition rate. The RF phase is transferred to the optical signal in the AOM and thus to the photo-detected beat wave. Phase locking the AOM drive to the laser repetition rate enables the sampling oscilloscope, triggered on the repetition rate, to capture each interleaved pulse with an identical beat signal phase relative to the pulse envelope. This step prevents fringe washout in the recorded waveform. The locking would not be necessary if a real-time, non-interleaved digitizer were used, and a single pulse were acquired. As before, the signal and reference pulses are routed to both the fast photodiode and the OSA for comparison of time domain OFDR against conventional OFDR.

Typical data demonstrates the decoupling approach. To improve visual clarity, detected waveforms with low beat frequency are shown in Fig. 4.7. Pulses reflected from the blue and the red sides of the grating are drawn in blue, Fig. 4.7(a) and 4.7(c), and red, 4.7(b) and 4.7(d), respectively. In the time domain data the pulse reflected from the blue side of the CFBG, Fig. 4.7(a), shows a Doppler-induced increase in beat frequency relative to the pulse reflected from the red side, Fig. 4.7(b). The waveforms are also time reversed with respect to one another confirming the arrival of either the blue or red ends of the spectrum first. As chromatic dispersion is seen here to map frequency information to the time domain, it is not surprising that the same Doppler-Range phenomenon is observed in the frequency-domain data captured by the OSA and reproduced in Figs. 4.7 (c) and (d). Doppler–Range decoupling is a potentially compelling reason to utilize chirped femtosecond sources, as opposed to broadband cw sources, in conventional

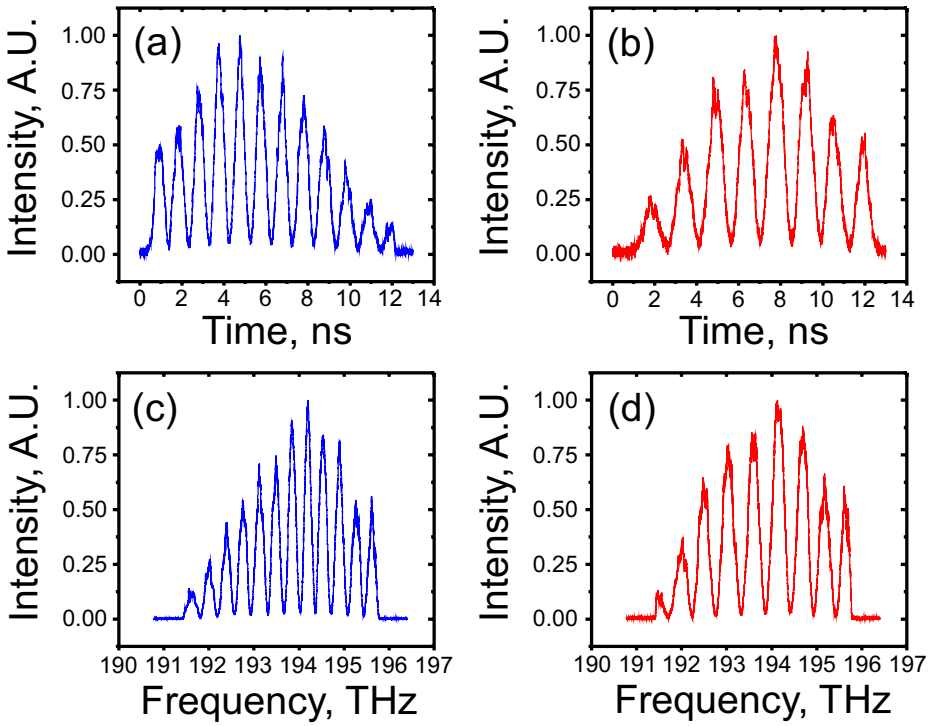

Fig. 4.7: Detected waveforms captured from a single reflection point at close range. Blue lines, (a) and (c), are obtained with pulses dispersed from the blue side of the CFBG, red lines, (b) and (d), with pulses dispersed form the red side. (a) and (b) show time domain data collected by the oscilloscope. Waveform time reversal is evident, as is the difference in beat frequency between (a) and (b) caused by Doppler-range coupling. (c) and (d) show spectral intensities as captured by the OSA. These two waveforms are similarly oriented but, like there time domain equivalents, exhibit Doppler-range coupling.

OFDR. However, as noted above, strict phasing requirements for the beat signal were imposed in this demonstration due to multi-pulse acquisition in time and frequency domains. To apply this technique generally to conventional OFDR, the spectrometer should acquire only one pulse per integration window.

Figure 4.8 depicts a 20 point scan over a centimeter worth of delays with constant 60 micron up and downshifts in the observed data from the blue and red ports, see upper inset figure. The green line represents the measured true range obtained by averaging the two measurements, R_1 and R_2, described in Eq. (4.13). The lower inset plot (obtained in another 55 point scan over centimeter range) shows the Doppler shift computed by

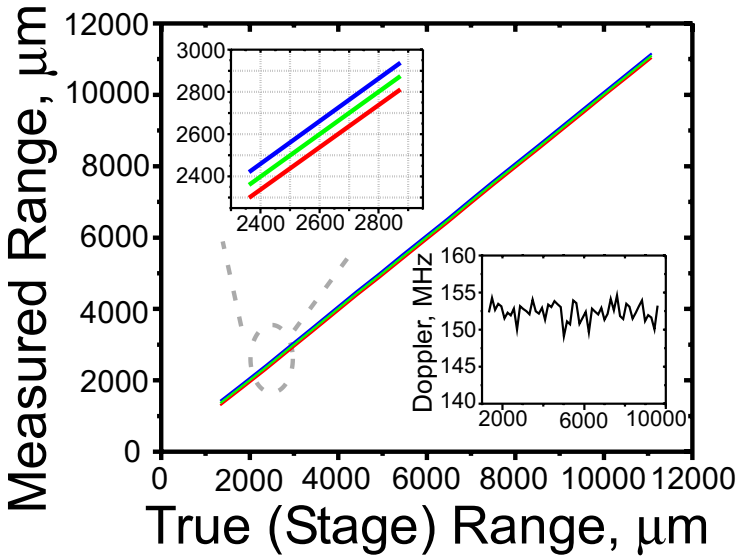

Fig. 4.8: Apparent range values measured for different true ranges (delay stage positions). The blue and red lines correspond to pulses dispersed from the blue and red sides of the CFBG, respectively. The green line is the weighed average of these two, which is the measured true range. The ±60 micron offsets of the blue and red lines resulting from coupling of the +152 MHz Doppler shift into the range measurement are visible in the upper inset. The lower inset shows the Doppler frequency determined from the difference between blue and red curves in a similar scan with higher sampling density.

subtracting R_2 from R_1. As expected the value is nearly constant at +152 MHz. As was the case in the earlier demonstration, chirp rates differ slightly from those of the CFBG due to fiber patch cables used in the setup. For the purpose of calculating true range (green curve in Fig. 4.8) and the Doppler shift, a chirp rate of -432.6 ps^2 is assumed for the blue port and 430.8 ps^2 for the red port. The raw readings of R_1 and R_2 are weighted accordingly. Good agreement is seen between measured data and the specifications of the demonstrator setup.

4.4 Doppler Immunity

While Doppler information is often desirable, as in functional OCT [87,88], and was shown separable in the previous section, some range-sensitive imaging systems may

wish to simply remove the effect to enhance image clarity. Earlier work in OCT showed that limiting the temporal duration of broadband signals or simply limiting the instantaneous duration of each frequency component within a swept source can greatly reduce Doppler blurring [89]. The former method physically limits the optical interaction time with a moving sample while the second utilizes post-processing to recreate a short interaction. A hybrid of these two solutions for Doppler immunity is easily implemented directly in the physical domain of a dispersion based time domain OFDR signal processor. A system variant in which the target pulse is dispersed after, rather than before, bouncing off the target proves Doppler-immune. In this case, the target pulse interacts with the moving sample over a limited time aperture but, due to the use of passive dispersion before photo-detection, can be ultimately received as a much longer frequency swept signal suitable for time domain OFDR. We compare the time-frequency mapping of pulses dispersed before and after a Doppler shift to clarify the difference between the two system configurations, and we demonstrate high-speed, Doppler-immune, dispersion-last ranging.

Despite the linearity of the dispersion based time domain OFDR system, a pulse Doppler shifted first and subsequently dispersed has a distinctly different instantaneous frequency profile than one first dispersed and then Doppler shifted. To derive the former, a Doppler shift is introduced through the factor, α, as in Eq. (4.9), to a Gaussian pulse. We write:

$$E(t') = \alpha E_0 \int_{-\infty}^{\infty} e^{-\frac{1}{2}\frac{(\Omega-\omega_c)^2}{(\Delta\omega)^2}} e^{j\Omega\alpha t'} d\Omega = E_0 \int_{-\infty}^{\infty} e^{-\frac{1}{2}\frac{(\Omega-\alpha\omega_c)^2}{(\alpha\Delta\omega)^2}} e^{j\Omega t'} d\Omega \qquad (4.12)$$

where a change of variables, $\Omega = \alpha\Omega$, was used on the right side. If chromatic dispersion is introduced as a quadratic spectral phase as in Eq. (4.8), a change of time variable, $t'' = t' - \Phi_2(\alpha - 1)\omega_c$, facilitates completing the square and integrating to yield:

$$E(t') = \frac{\sqrt{2\pi}E_0 e^{-j\frac{1}{2}\Phi_2(1-\alpha^2)\omega_c^2}}{\sqrt{(\alpha\Delta\omega)^{-2} + j\Phi_2}} e^{j\alpha\omega_c t''} e^{-\frac{1}{2}\frac{t''^2}{(\alpha\Delta\omega)^{-2}+j\Phi_2}} \approx Ce^{-\frac{1}{2}\frac{t''^2}{(\alpha\Delta\omega)^2\Phi_2^2}} e^{j\left(\alpha\omega_c t'' + \frac{1}{2}\frac{t''^2}{\Phi_2}\right)}. \quad (4.13)$$

Here again we utilize the approximation, $1/\Delta\omega^2 \ll \Phi_2$ to simplify the exponentials. A derivative of the temporal phase produces an instantaneous frequency,

$$\Omega_{inst}(t'') \approx \alpha\omega_c + \frac{t''}{\Phi_2},\ \Omega_{inst}(t') \approx \alpha\omega_c + \frac{t' - \Phi_2(\alpha-1)\omega_c}{\Phi_2} = \omega_c + \frac{t'}{\Phi_2}, \quad (4.14)$$

identical to that for the dispersed only (i.e. non-Doppler) pulse treatment of Eq. (4.3). It should be noted, however, that the Doppler terms do not entirely drop out without the approximation $1/\Delta\omega^2 \ll \Phi_2$.

An intuitive explanation for the Doppler immunity may be offered as follows. When a transform limited broadband pulse is subjected to a small Doppler shift, it merely changes the upper and lower limits of the pulse spectrum. The central components shift as well but are replaced in their former position by a neighboring component. Due to the linearity of the spectral phase of the pulse, all spectral components remain collocated at the temporal position, Φ_1, of the original carrier frequency. Consequently, except near the margins of the spectrum, the Doppler shifted pulse performs in subsequent processing identically to a pulse that has not been Doppler shifted. When the beat frequency is

generated between a dispersed reference pulse and a delayed copy of the target pulse of Eq. (4.14), the signal reflects only range information.

The treatment leading to Eq. (4.14) assumed an interaction of a transform-limited pulse with the target. In some applications this approach may be power limited by the maximum permissible exposure of the sample before ensuing damage occurs. For metrology with these target samples, a pre-stretching scheme would allow for greater average powers and/or reduced peak powers. The lack of transform limited incidence for the target pulse, however, implies that some Doppler-range coupling will occur. The factor introduced in Section 4.3, $\Phi_2 c\pi$, describes the ratio of range adjustment to Doppler frequency. If a pre-stretch technique were employed, the net suppression of Doppler-range coupling would be limited to a factor of $\Phi_{2\_CFBG}/\Phi_{2\_Pre\text{-}stretch}$. As an example, tens of meters of patch cables will pre- stretch the 150fs pulses used here to the ten picosecond scale. The peak power drops by a factor of 100 while Doppler suppression remains greater than 20dB as $\Phi_{Pre\text{-}stretch} \approx 1\text{ps}^2$.

To confirm the Doppler immunity of the dispersion-last approach, our experimental system in Fig. 4.6 is modified by exchanging the order of the switch box, circulator, and CFBG with the Mach-Zehnder interferometer. All other system parameters are unchanged. Fig. 4.9 shows sample waveforms, organized akin to Fig. 4.7, taken by the oscilloscope and OSA under short relative delay and +152 MHz Doppler shift. Signals dispersed from either side of the CFBG exhibit the same beat frequency. A slight discrepancy between visualized beat frequency for the blue and red conventional OFDR waveforms is attributable to phase drift of the interferometer (and the beat signal)

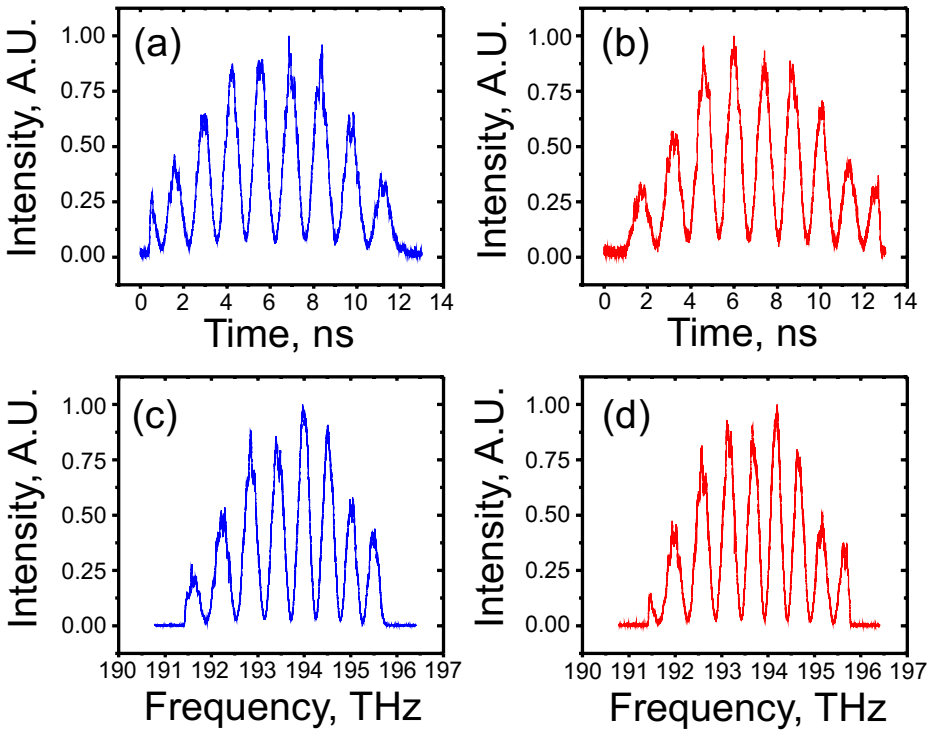

Fig. 4.9: Single reflection point waveforms captured with the dispersion-last system and presented as in Fig. 7. No Doppler-range coupling is present; all signals exhibit the same beat under their envelopes. Interferometric phase drift over the duration of the spectral scan results in the small beat deviation in (c) and (d) with respect to (a) and (b).

during the several-second duration OSA scans. Note again the time reversal of the envelopes captured by the oscilloscope. Fig. 4.10 shows a 55 point range scan demonstrating the overlap of data taken from the blue and red side of the CFBG. The difference between R_1 (blue line) and R_2 (red line) range values is on the order of 1μm, compared to ~120μm for the Doppler-first configuration, Fig. 4.8. Due to the strong agreement, a weighted average (measured true range) is not presented. If a Doppler shift were to be computed from this difference, as in Fig. 4.8 lower inset, the apparent Doppler frequency would be close to zero. This effect is illustrated inset in Fig. 4.10, where all apparent Doppler values are under 4 MHz with an average of 1.3 MHz, two orders of magnitude below the 152 MHz actual Doppler shift present. Comparing the results of

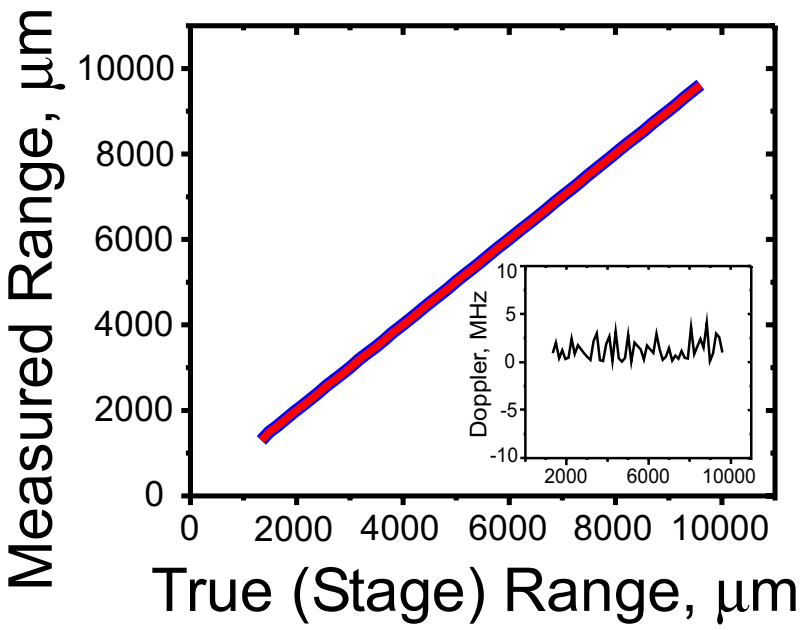

Fig. 4.10: Apparent range values measured for different true ranges (stage delay positions). The blue and red lines correspond to pulses dispersed from the blue and red sides of the CFBG, respectively. The blue line is drawn thicker to permit viewing. Agreement between the two measured ranges for each true range is on the order of 1μm. The inset shows the perceived Doppler shift, which is < 4MHz at all points, a significant reduction from the imposed +152 MHz shift.

Figs. 4.8 and 4.10, good agreement exists between theory and observation. While the data of Fig. 4.10 is all based on time domain detection, similar results were observed using conventional OFDR by OSA detection. A ranging system could clearly be designed with Doppler immunity if it were tolerable to transmit and receive short pulses, withholding most dispersion until the return of the target and reference pulses. The approach highlights the unique capability that chromatic dispersion offers for passive generation of high-speed, broadband frequency sweeps with low loss at any point of the processing chain. This approach to chirp signal generation is more flexible than actively swept source technology, which must drive the system from the launch.

4.5 Summary and Acknowledgement

Several enhancements to the time domain realization of OFDR through the introduction of a linear CFBG as means for high-speed chirp generation are demonstrated. The utility of the CFBG is shown in the realization of a moderate/low resolution surface scan with a near-theoretically-limited number of resolvable spots. The idealized signal dispersion offered by the linear CFBG gives single point dynamic range matching that of earlier demonstrated systems based on frequency swept signals derived from dispersed short pulses despite the removal of potentially accuracy spoiling interpolative post-processing. A novel system arrangement is implemented with a two pulse sequence generated by dispersing the launch pulse from both ends of the same linear CFBG in succession. This approach permits the decoupling and isolation of Doppler and range information with maximum contrast. A further alteration leads to system operation in a dispersion-last approach providing Doppler-immune range values.

While time domain OFDR based on dispersed wideband pulses has disruptive potential, certain key technical challenges lie in its path. The use of linear CFBGs is restricted to systems with moderate numbers of resolvable spots until critical improvements to grating fabrication are implemented. Techniques to reduce amplitude and phase ripple, which impact system DR, and methods to further lengthen CFBGs to increase dispersion values and operating bandwidths are essential. Of equal importance, fast A/D converters are a gateway to extending the number of resolvable spots in real time operation. Current technological limits will restrict dispersion based time domain OFDR to mm ranges until A/D converters at several GHz can offer sufficient dynamic

range. The creation of highly stable broadband sources through supercontinuum generation or other means centered at wavelengths appropriate to targets of interest and where low loss dispersive fiber technologies exist is a last technical step. As enabling technologies improve, a time domain OFDR system based on dispersion of short pulses with micron scale resolution over a centimeter range utilizing a sub microsecond time aperture should emerge.

The text of Chapter Four, in part, is a reprint of the material as it appears in:

R. E. Saperstein, N. Alic, S. Zamek, K. Ikeda, B. Slutsky, and Y. Fainman, "Processing advantages of linear chirped fiber Bragg gratings in the time domain realization of optical frequency-domain reflectometry," Opt. Express **15**, 15464-15479 (2007).

The dissertation author was the primary researcher and author. The co-authors listed in this publication directed and supervised the research that forms the basis for this chapter.

Chapter 5

Conclusion

5.1 Summary

This dissertation presents an investigation of longitudinal spectral decomposition of ultrashort pulses, which is aimed at identifying and exploring information processing applications. The creation and manipulation of longitudinal SDWs are treated theoretically and practically. Special emphasis is placed on the opportunities and limits imposed by available technologies. Specifically, technologies developed for fiber optic telecommunications are leveraged throughout this work. Sources of chromatic dispersion in fiber are compared, and advantages of each of the different approaches are highlighted. Fiber cable as a dispersion source is promoted for its widespread availability and low cost. In these fibers polarization properties are manageable (especially in DCF), but higher order dispersion terms can prove quite strong over operational bandwidths of interest. CFBGs are an alternative choice, where tailoring of the spectral response can remove major higher order terms at the expense of introducing group delay ripple. CFBGs have also shown the best dispersion to loss ratios of any technology investigated. The

principle drawback to their widespread usage in longitudinal SDW processing is their higher order PMD. This effect limits their use to only the reflectometry application of Chapter 4. As each of the included dispersion technologies improves, it will enable further signal processing gains. Of particular interest to the applications in this dissertation is the creation of polarization maintaining CFBGs that eliminate the PMD issue and allow EO modulation of CFBG induced longitudinal SDWs. However, it should be emphasized that many dispersion source specifications need addressing. As an example, additional improvements to the CFBG writing process should center on adding to the total grating length and minimizing/removing group delay ripple. Without these changes, high quality longitudinal SDW generation over broad bandwidths will remain impossible in CFBGs.

Three applications of longitudinal SDW processing are discussed in this dissertation. The first looks at the ability to shape the waveform of optical pulses with detail on the sub-picosecond time scale. The approach uses the similarity of spectral and temporal linear phase shifts within longitudinal SDWs to create delayed and weighted copies of the original short pulse through microwave signal modulation. The total number of resolvable spots is shown to be heavily impacted by third order dispersion. The second application analyzes and synthesizes microwave signals through the coherent mixing of manipulated longitudinal SDWs. A basic processing unit, the asymmetric Mach-Zehnder interferometer, is shown to allow for the mixing of microwave signals with user defined, delay-tuned beat signals. Through variations of the optical detection scheme, this mixing works as a projection to perform analysis, or as a simple product to introduce independent envelope and carrier signals. Again third order dispersion impacts

the system through the distortion of the controllable microwave beat frequency. The last application uses longitudinal SDWs as extremely fast frequency swept sources in the time domain realization of OFDR. A coherent detection scheme produces a measurable IF, as in the microwave photonic approaches, which when analyzed and scaled, directly gives target range. High speed ranging/imaging of targets with moderate resolution is accomplished while CFBGs are shown to both simplify and extend signal processing. Other recent results from the literature are closely compared to emphasize the role that linear CFBGs add to longitudinal SDW processing as compared to chromatic dispersion sources with higher order dispersion.

5.2 Future Directions

Looking forward, longitudinal SDW processing will only improve as the underlying technologies involved in dispersion, modulation, and detection increase in performance. For instance, the high speed electronics involved in modulation, signal detection, and signal digitization are constantly scaling to higher frequencies and increasing dynamic range. For microwave-photonic applications, when these electronic technology improvements are incorporated, longitudinal SDW based processing becomes more powerful. And because photonics here serves to extend the capability of electronics, the relevance and necessity of this processing is maintained. This effect is nowhere more evident currently than in the longitudinal SDW-assisted A/D conversion work performed elsewhere [62]. Incorporation of larger fractional bandwidth optical pulses is also an exciting opportunity space for longitudinal SDWs. Supercontinuum sources are an option in this direction, where the implications of bandwidth increase must be weighed

out. Specifically, the question of interest is whether the gains in processing ability overcome the challenge of creating controllable phase responses over such large spectral regions. If added, broadband sources should allow for the pushing of demonstrated microwave-photonic applications toward millimeter wave speeds. Additionally incorporation of supercontinuum sources into the time domain OFDR demonstration allows for tomography and imaging of biological materials with micron scale depth resolution. While electronic processing enhancements and supercontinuum incorporation are forthcoming, examples exist of technology initiative currently underway. For instance, preliminary characterization of CFBGs written in polarization maintaining fibers indicate that their performance does offer anticipated reduction in spectral polarization rotation. Longer gratings are in design at this time to truly replicate commercial CFBG offerings and to validate the PM fiber approach. From this brief survey, it is apparent that technology improvement will clearly play a large roll in advancing the roll of longitudinal SDW processing.

Additional application spaces should also open to longitudinal SDWs. One area of particular interest is the field of nonlinear optical spectroscopy. Specifically, the narrow instantaneous frequency of dispersed pulses is appealing for spectral selectivity and chemical specificity in resonant nonlinear interactions. Initial work on spectral focusing in nonlinear optics with longitudinal SDWs was shown in Refs. 21, 22, and 70. The former two references make use of the IF generated by delayed longitudinal SDWs to create a vibrational or rotational coherence in an ensemble of molecules. A probe pulse can scatter of this ensemble and receive an energy up-shift relating to the vibrational or rotational level. This form of spectroscopy is called coherent anti-Stokes

Raman scattering. By changing the delay tuned IF, the levels of the molecules and their relative populations can be mapped out. These factors are important for both molecular identification and thermometry. The two earlier demonstrations utilize free space components to generate chirped pulses, but fiber based chromatic dispersion has the ability to greatly enhance spectral selectivity through increased dispersion accumulation. In conjunction with resonant TPA fluorescence [90-91], the approach of Ref. 70, using counter-phased longitudinal SDWs mixing under delay, could also produce very exciting results in nonlinear microscopy. Here the sum frequency from two counter phased (oppositely frequency swept) SDWs results in a narrowband quasi-monochromatic frequency at roughly twice the optical carrier frequency. Changing the relative delay between SDWs tunes the sum frequency through a spectral region of interest. For an appropriate molecule, TPA will occur for a particular delay and sum frequency. The event is recorded by the microscope after a fluorescence emission relaxation event is detected. In this way the locations of a particular florescent (or fluorophore-tagged) biological molecule can be imaged using fluorescence. In both nonlinear spectroscopy approaches, care must be taken to balance the amount of dispersion to achieve appropriate spectral selectivity while maintaining sufficient instantaneous power levels.

In a second exciting application, longitudinal SDWs can be used to facilitate the implementation of a covert, actively illuminated imaging system. Active illumination systems have particular advantages over passive systems in particular as the source coherence is controllable and the range to target is readily obtained. In order to promote covertness, a signal must be hidden below the background noise levels of other radiation sources (i.e. the sun, etc.). The use of modelocked ultrafast lasers is ideal for distributing

signal energy in the spectral domain. The source can be operated such that its power spectrum exists below solar background. However, temporal confinement of signal energy makes these pulses readily distinguishable from solar radiation, thus eliminating covertness. To spread the signal in time as well as frequency, chromatic dispersion can be used to convert short pulses to longitudinal SDWs. Because the dispersion is passive, the target could still readily reconstruct a short pulse simply by maximizing the peak power of the dispersion compensated illumination signal. To add security and support higher levels of covertness, the longitudinal SDW can be imprinted with a high speed temporal phase code before illumination. This coding process is akin to the use of temporal phase chips in OCDMA signaling. The temporal modulation adds a degree of active randomness to the illumination signal ensuring the target cannot isolate it from the incoherent background. The use of time domain modulation further ensures security by allowing the phase code to be actively changed on a pulse-to-pulse basis. Temporal signal variance implies that sophisticated target processing cannot be used to reconstruct the illumination pulse. However, at the detector, the return signal can be reconstructed using conjugate OCDMA temporal phase and dispersive spectral phase codes. With the phase linearized, the energy of the return collocates in time to create a pulse that is distinguishable from the background radiation through a time gating or nonlinear filtering operation. The return can ultimately be used for covert three dimensional imaging of the target. The principle challenge to the implementation is the need to eliminate the temporal phase code through multiplication in time with a conjugated phase signal. The approach requires time synchronize between the application of the conjugate OCDMA phase code with the return pulse envelope arrival. For temporal SDWs on the 10 ns scale,

a 128 chip code would require synchronization at the tens of picosecond scale. When target range is not first known, the synchronization would be particularly challenging because of a lack of available signal energy to derive a clock from. The challenges of the implementation make the project well suited for a speculative academic venture.

In all, longitudinal SDWs are a unique processing approach for linear or nonlinear interactions and should be considered a standard method in the ultrafast signal processing toolbox. Through descriptive examples the manuscript has shown that sufficient technologies currently exist to perform extensive processing techniques, while further technology improvement will serve to strengthen these capabilities.

Bibliography

[1] See as example of modelocked laser providers: Coherent Inc., www.coherent.com, Spectra-Physics, www.spectraphyics.com, KMLabs Inc., www.kmlabs.com, IMRA America, Inc., www.imra.com, PriTel, Inc., www.pritel.com.

[2] D. Slepian, "On Bandwidth," Proc. IEEE 64, 292-300 (1976).

[3] A. M. Weiner, J.P. Heritage, and E. M. Kirschner, "High-resolution femtosecond pulse shaping," J. Opt. Soc. Am. B **5**, 1563-1572 (1988).

[4] J-C. Diels and W. Rudolph, *Ultrashort Laser Pulse Phenomenon*, Academic Press, San Diego, 1996.

[5] A. M. Weiner, D. E. Leaird, J. S. Patel, and J. R. Wullert II, "Programmable shaping of femtosecond optical pulses by use of 128-element liquid crystal phase modulator," J. Quantum Electron. **28**, 908-920 (1992).

[6] M. A. Dugan, J. X. Tull, and W. S. Warren, "High-resolution acousto-optic shaping of unamplified and amplified femtosecond laser pulses," J. Opt. Soc. Am. B **14**, 2348-2358 (1997).

[7] T. Kurokawa, H. Tsuda, K. Okamoto, K. Naganuma, H. Takenouchi, Y. Inoue, and M. Ishii, "Time-space-conversion optical signal processing using arrayed-waveguide grating," Electron. Lett. 33, 1890-1891 (1997).

[8] M. M. Wefers and K. A. Nelson, "Space-time profiles of shaped ultrafast optical waveforms," IEEE J. Quantum Electron. **32**, 161-172 (1996).

[9] D. E. Leaird, A. M. Weiner, S. Kamei, M. Ishii, A. Sugita, and K. Okamoto, "Generation of flat-topped 500-GHz pulse bursts using loss engineered arrayed waveguide gratings," IEEE Photon. Technol. Lett. **14**, 816-818 (2002).

[10] A. Papoulis, "Pulse compression, fiber communications, and diffraction: a unified approach," J. Opt. Soc. Am. A. **11**, 3-13, (1994).

[11] Y. C. Tong, L. Y. Chan, and H. K. Tsang, "Fiber dispersion or pulse spectrum measurement using a sampling oscilloscope," Electron. Lett. **33**, 983-985 (1997).

[12] A. M. Weiner and J. P. Heritage, U.S. Patent No. 4,928,316, "Optical systems and methods based upon temporal stretching, modulation, and recompression of ultrashort pulses.

[13] M. Haner and W.S. Warren, "Synthesis of crafted optical pulses by time domain modulation in a fiber-grating compressor," Appl. Phys. Lett. **52**, 1548-1550 (1988)

[14] R. E. Saperstein, N. Alic, D. Panasenko, R. Rokitski, and Y. Fainman, "Time-domain waveform processing using chromatic dispersion for temporal shaping of optical pulses," J. Opt. Soc. Am. B **22**, 2427-2436 (2005)

[15] R.E. Saperstein, D. Panasenko, and Y. Fainman, "Demonstration of a microwave spectrum analyzer based on time-domain optical processing in fiber." Opt. Lett. **29**, 501-503 (2004)

[16] R. E. Saperstein and Y. Fainman, "Information processing with longitudinal spectral decomposition of ultrafast pulses," Appl. Opt., doc. ID **82277** (posted 14 August 2007, in press)

[17] J. Chou, Y. Han, and B. Jalali, "Adaptive RF-photonic arbitrary waveform generator," IEEE Phot. Tech. Lett. **15**, 581-583 (2003)

[18] J. D. McKinney, I.-S. Lin, and A. M. Weiner, "Shaping the Power Spectrum of Ultra-Wideband Radio-Frequency Signals," IEEE Trans. Micro. Theor. Tech. **54**, 4247-4255 (2006)

[19] J. Azaña, N. K. Berger, B. Levit, V. Smulakovsky, and B. Fischer, "Frequency shifting of microwave signals by use of a general temporal self-imaging (Talbot) effect in optical fibers," Opt. Lett. **29**, 2849-2851 (2004)

[20] B. H. Kolner, "Space-time duality and the theory of temporal imaging," IEEE J. Quant. Electron., **30**, 1951-1963 (1994)

[21] E. Gershgoren, R.A. Bartels, J.T. Fourkas, R. Tobey, M.M. Murnane, and H.C. Kapteyn, "Simplified setup for high-resolution spectroscopy that uses ultrashort pulses," Opt. Lett. **28**, 361-363 (2003).

[22] T. Hellerer, A. M.K. Enejder and A. Zumbusch, "Spectral focusing: High spectral resolution spectroscopy with broad-bandwidth laser pulses," Appl. Phys. Lett. **85**, 25-27 (2004).

[23] S. Lee, K. Kim, and P. J. Delfyett, "Extreme Chirped Pulse Oscillator (XCPO) Using a Theta Cavity Design," IEEE Photonics Tech. Lett, **18**, 799-801, (2006)

[24] S. Moon and D. Y. Kim, "Ultra-high-speed optical coherence tomography with a stretched pulse supercontinuum source," Opt. Express **14**, 11575-11584 (2006).

[25] Y. Park, T-J Ahn, J-C Kieffer, and J. Azaña, "Optical frequency domain reflectometry based on real-time Fourier transformation," Opt. Express **15**, 4598-4617 (2007).

[26] R. Saperstein, N. Alic, S. Zamek, K. Ikeda, B. Slutsky, and Y. Fainman, "Processing Advantages of chirped fiber Bragg gratings in the time domain realization of optical frequency domain reflectometry," Opt. Express. In press. (2007)

[27] X. Wang and N. Wada, "Spectral phase encoding of ultra-short optical pulse in time domain for OCDMA application," Opt. Express **15**, 7319-7326 (2007)

[28] J. Sharping, Y. Okawachi, J. van Howe, C. Xu, Y. Wang, A. Willner, and A. Gaeta, "All-optical, wavelength and bandwidth preserving, pulse delay based on parametric wavelength conversion and dispersion," Opt. Express **13**, 7872-7877 (2005)

[29] J. Ren, N. Alic, E. Myslivets, R. E. Saperstein, C. J. McKinstrie, R. M. Jopson, A. H. Gnauck, P. A. Andrekson and S. Radic, "12.47ns Continuously-Tunable Two-Pump Parametric Delay," European Conference on Optical Communication 2006 Postdeadline **Th4.4.3.** (2006)

[30] G. P. Agrawal, *Applications of Nonlinear Fiber Optics*, Academic Press, San Diego, 2001.

[31] Advanced Optical Solutions, www.aos-fiber.com, *note that 3M Corp. no longer produces CFBGs*

[32] Proximion Fiber Systems AB, http://www.proximion.com/

[33] M. Durkin, M. Ibsen, M. J. Cole, and R. I. Laming, "1m long continuously-written fiber Bragg grating for combined second- and third-order dispersion compensation," Electron. Lett. **33**, 1891-1893 (1997).

[34] P. Petropoulos, M. Ibsen, A.D. Ellis, and D. J. Richardson, "Rectangular pulse generation based on pulse reshaping using a superstructured fiber Bragg grating," J. Lightwave Technol. **19**, 746-752 (2001).

[35] S. Longhi, M. Marano, P. Laporta, O. Svelto, and M. Belmonte, "Propagation, manipulation, and control of picosecond optical pulses at 1.5 m in fiber Bragg gratings," J. Opt. Soc. Am. B **19**, 2742–2757 (2002).

[36] J. Azaña and L. R. Chen, "Synthesis of temporal optical waveforms by fiber Bragg gratings: a new approach based on space-to-frequency-to-time mapping," J. Opt. Soc. Am. B **19**, 2758–2769 (2002).

[37] X. Wang, K. Matsushima, K. Kitayama, A. Nishiki, N. Wada, and F. Kubota, "High-performance optical code generation and recognition by use of a 511-chip, 640-Gchip/s phase-shifted superstructured fiber Bragg grating," Opt. Lett. **30**, 355-357 (2005).

[38] P. C. Chou, H. A. Haus, and J. F. Brennan III, "Reconfigurable time-domain spectral shaping of an optical pulse stretched by a fiber Bragg grating," Opt. Lett. **25**, 524-526 (2000).

[39] D. Goldstein, *Polarized Light, 2nd Ed*. Marcel Dekker, New York, 2005.

[40] E. P. Wigner, "On quantum correction for thermodynamic equilibrium," Phys. Rev. **40,** 749–759 (1932).

[41] K. Wolf, D. Mendlovic, and Z. Zalevsky, "Generalized Wigner function for the analysis of superresolution systems," Appl. Opt. **37**, 4374-4379 (1998)

[42] W. S. Warren, H. Rabitz, and M. Dahleh, "Coherent Control of Quantum Dynamics: The Dream is Alive," Science **259**, 1581-1589 (1993).

[43] J. A. Salehi, A. M. Weiner, and J. P. Heritage, "Coherent ultrashort light pulse code-division multiple-access communication systems," J. Lightwave Technol. **8**, 478-491 (1990).

[44] P.-C. Sun, Y. Mazurenko, W. S. C. Chang, P. K. L. Yu, and Y. Fainman, "All Optical Parallel-to-serial Conversion by Holographic Spatial-to-Temporal Frequency Encoding," Opt. Lett., 20, 1728-1730 (1995).

[45] P. C. Sun, Y. Mazurenko, Y. Fainman, "Femtosecond pulse imaging: ultrafast optical oscilloscope," JOSA A, 14, 1159-1169, (1997)

[46] P. C. Sun, Y. Mazurenko, Y. Fainman," Real-time 1-D Coherent Imaging Through Single-mode Fibers by Space-Time Conversion Processors," Opt. Lett., 22, 1861-1863, (1997)

[47] D. M. Marom, D. Panasenko, P.-C. Sun, and Y. Fainman, "Spatial-temporal wave mixing for space-to-time conversion," Opt. Lett. 24, 563-565 (1999).

[48] D. M. Marom, D. Panasenko, R. Rokitski, P.-C. Sun, and Y. Fainman, "Time reversal of ultrafast waveforms by wave mixing of spectrally decomposed waves," Opt. Lett. 25, 132-134 (2000).

[49] D. Marom, D. Panasenko, P. C. Sun, Y. Fainman, "Femtosecond rate space-to-time conversion," J. Opt. Soc. Am.: B, 17, 1759-73, (2000)

[50] D. Marom, D. Panasenko, P. C. Sun, Y. Fainman, "Linear and Nonlinear Operation of a Time-to-Space Processor," J. Opt. Soc. Am.: A, 18, 448-458, (2001)

[51] D. Marom, D. Panasenko, P. C. Sun, Y. Mazurenko, Y. Fainman, "Real-Time Spatial-Temporal Signal Processing with Optical Nonlinearities," IEEE Journal of Selected Topics in Quantum Electronics, v. 7, No. 4, pp. 683-693, (2002)

[52] S. Shen, C. C. Chang, H. P. Sardesai, V. Binjrajka, and A. M. Weiner, "Effects of Self-Phase Modulation on Sub-500 fs Pulse transmission over Dispersion Compensated Fiber Links" J. Lightwave Technol., **17**, 452 (1999)

[53] G. P. Agrawal, *Nonlinear Fiber Optics*, 3rd ed. Academic Press, San Diego, 2001

[54] J. van Howe and C. Xu, "Ultrafast optical delay line by use of a time-prism pair," Opt. Lett. **30**, 99-101 (2005).

[55] Y. Takagi, T. Kobayashi, K. Yoshihara, and S. Imamura, "Multiple- and single-shot autocorrelator based on two-photon conductivity in semiconductors," Opt. Lett. **17**, 658-660 (1992).

[56] L. F. Mollenauer, P. V. Mamyshev, J. Gripp, M. J. Neubelt, N. Mamysheva, L. Grüner-Nielsen, and T. Veng, "Demonstration of massive wavelength-division multiplexing over transoceanic distances by use of dispersion-managed solitons," Opt. Lett., **25,** 704-706 (2000).

[57] Evidence of the breadth of this topic is captured in the proceedings of the annual IEEE Microwave Photonics Conference. See for instance Proceedings of MWP 2007 (IEEE, Piscataway, NJ, 2007) or an alternate year. (online visit www.mwp2007.org).

[58] V. Lavielle, I. Lorgeré, J.-L. Le Gouët, S. Tonda, D. Dolfi, "Wideband versatile radio-frequency spectrum analyzer," Opt. Lett. **28**, 384-386 (2003)

[59] A. S. Weling, B. B. HLI, N. M. Froberg, and D. H. Auston, "Generation of tunable narrow-band THz radiation from large aperture photoconducting antennas," Appl. Phys. Lett. **64**, 137-139 (1994).

[60] H. Zmuda, E. N. Toughlian, *Photonic Aspects of Modern Radar*, Artech House, Boston, 1994.

[61] B. B. Hu, M. C. Nuss, "Imaging with terahertz waves," Opt. Lett. **20**, 1716-1718 (1995).

[62] G. C. Valley, "Photonic analog-to-digital converters," Opt. Express **15**, 1955-1982 (2007)

[63] D. Panasenko and Y. Fainman, "Interferometric correlation of infrared femtosecond pulses with two-photon conductivity in a silicon CCD," Appl. Opt. **41**, 3748-3752 (2002).

[64] M. Ghavami, L. B. Michael, and R. Kohno, *Ultra-wideband Signals and Systems in Communication Engineering*, John Wiley & Sons, Hoboken, NJ, 2004.

[65] J. U. Kang, M. Y. Frankel, and R. D. Esman, "Demonstration of microwave frequency shifting by use of a highly chirped mode-locked fiber laser," Opt. Lett. **23**, 1188-1190 (1998).

[66] J.D. McKinney, D. E. Leaird, and A. M. Weiner, "Millimeter-wave arbitrary waveform generation with a direct space-to-time pulse shaper," Opt. Lett. **27**, 1345-1347 (2002).

[67] S. Xiao, J. D. McKinney, and A. M. Weiner, "Photonic microwave arbitrary waveform generation using a virtually imaged phased-array (VIPA) direct space-to-time pulse shaper," IEEE Phot. Tech. Lett. **16**, 1936- 1938 (2004).

[68] T. Yilmaz, C. M. DePriest, T. Turpin, J. H. Abeles, and P. J. Delfyett, "Toward a photonic arbitrary waveform generator using a modelocked external cavity semiconductor laser," IEEE Phot. Tech. Lett. **14**, 1608-1610 (2002).

[69] D. Uttam and B. Culshaw, "Precision time domain reflectometry in optical fiber systems using a frequency modulated continuous wave ranging technique," IEEE J. Lightwave Technol. **3,** 971-977 (1985)

[70] E. Arons, E. N. Leith, A-C Tien, and R. Wagner, "High-resolution optical chirped pulse gating" Appl. Opt. **36**, 2603-2608 (1997)

[71] B. L. Stann, A. Abou-Auf; K. Aliberti; J. Dammann; M. Giza; G. Dang; G. Ovrebo; B. Redman; W. Ruff; and D. Simon., "Research progress on a focal plane array ladar system using chirped amplitude modulation," in Laser Radar Technology and Applications VIII, Gary Kamerman, Ed., Vol. 5086 of Proceedings of SPIE (SPIE, Bellingham, WA, 2003), 47-57

[72] S. Yun, G. Tearney, J. de Boer, N. Iftimia, and B. Bouma, "High-speed optical frequency-domain imaging," Opt. Express **11**, 2953-2963 (2003)

[73] R. Huber, M. Wojtkowski, K. Tiara, J. G. Fujimoto, and K. Hsu, "Amplified, frequency swept lasers for frequency domain reflectometry and OCT imaging: design and scaling principles," Opt. Express. **13**, 3513-3528 (2005)

[74] J. R. Klauder, A. C. Price, S. Darlington, and W. J. Albersheim, "The theory and design of chirp radars," Bell Syst. Tech. J. **39,** 745–808 (1960)

[75] D. A. Ausherman, A. Kozma, J. L. Walker, H. M. Jones, and E. C. Poggio, "Developments in radar imaging," IEEE Trans. Aerosp. Electron. Syst. **AES-20,** 382–384 (1984)

[76] C. V. Bennett and B. H. Kolner, "Aberrations in Temporal Imaging," IEEE J. Quant. Electron., **37**, 20-32 (2001)

[77] J. R. Birge, R. Ell, F.X. Kärtner, "Two-dimensional spectral shearing interferometry for few-cycle pulse characterization," Opt. Lett. **31**, 2063-2065 (2006)

[78] M. A. Muriel, J. Azaña, and A. Carballar, "Real-time Fourier transformer based on fiber gratings," Opt. Lett. **24,** 1-3 (1999)

[79] M. Wojtkowski, V. Srinivasan, T. Ko, J. Fujimoto, A. Kowalczyk, and J. Duker, "Ultrahigh-resolution, high-speed, Fourier domain optical coherence tomography and methods for dispersion compensation," Opt. Express **12**, 2404-2422 (2004)

[80] Y. Yasuno, V. D. Madjarova, S. Makita, M. Akiba, A. Morosawa, C. Chong, T. Sakai, K. -P. Chan, M. Itoh, and T. Yatagai, "Three-dimensional and high-speed swept-source optical coherence tomography for in vivo investigation of human anterior eye segments," Opt. Express **13**, 10652-10664 (2005)

[81] M. Sumetsky, B. Eggleton, and C. de Sterke, "Theory of group delay ripple generated by chirped fiber gratings," Opt. Express **10**, 332-340 (2002)

[82] S. Gee, S. Ozharar, F. Quinlan, and P. J. Delfyett, "Mode partition noise measurement of time stretched ultralow noise actively modelocked semiconductor based laser," Proceedings of the 2007 IEEE LEOS Annual Meeting, Paper ThD3, (IEEE, Piscataway, NJ, 2007)

[83] C. Dorrer, N. Belabas, J-P Likforman, and M. Joffre, "Spectral resolution and sampling issues in Fourier transform spectral interferometry," J. Opt. Soc. Am. B **17**, 1795-1802 (2000)

[84] A. W. Rihaczek, *Principles of High-Resolution Radar* (McGraw-Hill, Inc., 1969)

[85] S. H. Yun, G. Tearney, J. de Boer, and B. Bouma, "Motion artifacts in optical coherence tomography with frequency-domain ranging," Opt. Express **12**, 2977-2998 (2004)

[86] Y. C. Fung, *Biomechanics: Circulation, 2 ed.* (Springer-Verlag, 1997)

[87] T. G. van Leeuwen, M. D. Kulkarni, S. Yazdanfar, A. M. Rollins, and J. A. Izatt, "High-flow-velocity and shear-rate imaging by use of color Doppler optical coherence tomography," Opt. Lett. **24**, 1584-1586 (1999)

[88] A. H. Bachmann, M. L. Villiger, C. Blatter, T. Lasser, and R. A. Leitgeb, "Resonant Doppler flow imaging and optical vivisection of retinal blood vessels," Opt. Express 15, 408-422 (2007)

[89] S. H. Yun, G. Tearney, J. de Boer, and B. Bouma, "Pulsed-source and swept-source spectral-domain optical coherence tomography with reduced motion artifacts," Opt. Express **12**, 5614-5624 (2004)

[90] D. Meshulach and Y. Silberberg, "Coherent quantum control of two-photon transitions by a femtosecond laser pulse," Nature **396**, 239-242 (1998)

[91] D. Meshulach and Y. Silberberg, "Coherent quantum control of multiphoton transitions by shaped ultrashort optical pulses," Phys. Rev. A **60**, 1287-1292 (1999).